In vitro comparison of three percutaneous atrial septal defect closure devices for endothelialisation and haemocompatibility

Yael Levy, Zakaria Jalal, Audrey Aussel, Noélie B. Thebaud, Martine Renard, Reine Bareille, Jean Ripoche, Marlène Durand, Jean-Benoit Thambo, Laurence Bordenave

Yael Levy, Zakaria Jalal, Audrey Aussel, Noélie B. Thebaud, Martine Renard, et al.. In vitro comparison of three percutaneous atrial septal defect closure devices for endothelialisation and haemocompatibility. Archives of cardiovascular diseases, 2020, 113, pp.503 - 512. 10.1016/j.acvd.2020.03.022 . hal-03491669

HAL Id: hal-03491669
https://hal.science/hal-03491669v1

Submitted on 14 Sep 2022

A new insight on the analysis of residual stresses related distortions in selective laser melting of Ti-6Al-4V using the improved bridge curvature method

Mehdi Salem[a*], Sabine Le Roux[a], Anis Hor[b], Gilles Dour[c]

[a] Institut Clément Ader (ICA), Université de Toulouse, CNRS, Mines-Albi, ISAE-SUPAERO, UPS, INSA, Campus Jarlard, 81013 Albi CT, CEDEX 09, France
[b] Institut Clément Ader (ICA), Université de Toulouse, CNRS, Mines-Albi, ISAE-SUPAERO, UPS, INSA, 3 rue Caroline Aigle, 31400 Toulouse, France
[c] Present address: Advisian, Worley Parsons, Perth, Australia.
* Corresponding author
E-mail addresses: mehdi.salem@mines-albi.fr (M. Salem), sabine.leroux@mines-albi.fr (S. Le Roux), anis.hor@isae-supaero.fr (A. Hor), gretchgilles@netspace.net.au (G. Dour).

Abstract

Residual stresses are a major issue in the Selective Laser Melting process, which allows to build near net shape parts by stacking several thousand weld beads. This experimental study aims to investigate the relationships between process parameters and the part distortion. Based on the Bridge Curvature Method (BCM) and 3D topographic measurements of the top surface of the specimens, the effect of the volumetric energy density, the geometry and the scanning strategy are analyzed. The method and the proposed distortion criteria clearly highlight the anisotropy of the residual stress state, which depends on the direction and the speed of the scanning. The main curvature is oriented along scan direction for scanning speed higher than 1000 mm/s. The decrease in volumetric energy increases distortion, below a threshold value. The scan vector length, which can be varied by changing the scanning strategy and the specimen geometry, plays a primordial role on the residual stresses. The distortion amplitude decreases by shortening the scan vectors. Finally, the prospect of an adimensional analytical model taking into account the transient thermal gradient is given.

Keywords: Selective laser melting, residual stresses, scanning strategy, distortion, thermal stresses.

1. Introduction

Selective Laser Melting (SLM) is a power bed fusion technology that allows generating complex, near net-shape and lightweight 3D parts with near full density. This process consists in selectively melting successive layers of metallic powder on top of each other, using a high-power density laser [1]. Due to the highly localized energy input of the focused laser beam during very short interaction times, high residual stresses can occur in as-built components.

The generation of residual stresses has been described by Mercelis & Kruth, according to a mechanism in two stages including the Temperature Gradient Mechanism (TGM) and the cool-down phase [2]. In the first step, the rapid heating of the upper surface results in steep temperature gradients, followed by the relatively slow heat conduction through the material. As the expansion of the hotter material is restricted by the relatively colder underlying material, the upper layer undergoes compressive stresses whilst simultaneously the material strength is reduced due to the temperature rise. During the cool-down phase, thermal contraction lead to the shrinkage of the top layers which is restricted by the underlying material. Consequently, tensile stresses are introduced on the top layer and are balanced by compressive stresses below [1,3]. The release of these residual stresses during processing or after separation from the base plate can cause shape distortions, and even part failure by delamination or cracking [4-6]. It is therefore important to understand and control the residual stresses in order to optimize the SLM process.

Many studies reporting the influence of SLM process parameters on residual stresses can be found in the literature [6-9]. Some investigations deal with conventional in-process parameters such as the laser power [3,10-12], the scanning speed [3,10-14], the hatch distance [15] and the layer thickness [3-4,16-17]. Vrancken [3] reported that the laser power had the smallest effect on the residual stresses in comparison to either the laser scan speed or the layer thickness. However, correlations between these parameters and the residual stresses produced were difficult to establish, due to the variations in the size and dimensions of the melt resulting from fluctuating laser power during scanning, melt pool instabilities and heterogeneous powder bed [3,8]. Such process parameters are generally studied together as inputs to the volumetric energy density [3,7-8], which has actually no physical meaning, but is generally reported to reduce the residual stress as it increases [3,10,12,14]. However, as pointed out in [7], its effect on the residual stresses must be studied further to complement the little existing research on the subject.

Other work focuses on alternative parameters such the scanning strategy [2,4,10-11,13,17-28] including the re-scanning (also called re-melting or multiple scanning) [4,7,20,25,29], the height and/or preheating of the substrate plate [2,4,12,17,24,29-34], the inter-layer dwell time [12,16,35], the thickness or number of layers [2,5,34,36-38], and the support structures [39-42]. Through these works, it was generally concluded that a setting of parameters leading to a decrease in the temperature gradient, as for example the preheating of the base plate or the use of short scan vectors, reduces the level of the residual stresses [4,7,9-10,12,24-25,37]. Subsequent heat treatment can also be used to reduce residual stresses

[2,4,14,25,29,43-44]. However, such post-processing increases the production time and cost of the SLM components. Managing residual stress fields by optimizing in-process parameters therefore remains the most attractive solution. Despite the myriad of experimental works reported in the literature, these do not always provide a comprehensive and unambiguous insight of the effect of influencing parameters. In addition, the measurement of residual stresses is not obvious and various methods, either mechanical/destructive (such as hole drilling, layer removal, contour, part deformation, etc.), or physical/non-destructive (such as X-ray or neutron diffraction, ultrasonic or magnetic wave propagation, etc.), can be used [9,45]. The selection of the measurement technique depends on the nature of the specimen and the information required, namely the measurement depth (surface or thickness), the length scale to be measured (macroscopic, mesoscopic or microscopic), and the precision level resolution. Comparing reported results obtained by different techniques and analyzing the correlations between process parameters and the magnitude of residual stresses can therefore be confusing [3,8]. Residual stresses can be classified into different length scales: type I (which refers to macro-stresses which develop in the body of a component on a scale greater than the material grain size), type II (which vary on the scale of an individual grain, due to anisotropic material properties), and type III (which exist inside a grain, mainly due to the presence of dislocations and other crystal defects). Types II and III, which are often grouped together as "microscopic residual stresses", have a very limited effect on the mechanical properties of the material and are beyond the scope of most of the current measuring methods [2,3,9]. Distortion measurements can be used to assess indirectly and qualitatively - but quickly and inexpensively - the residual macroscopic stresses (type I) which vary continuously over a large distance in the part [4,42]. Such methods are based on the principle of "strain release", which consists in disturbing the mechanical equilibrium of the specimen by cutting to relax the residual stresses, and then measuring the deformed shape. The measured deformations can be input into Finite Element (FE) or analytical models to estimate the original stress state.

The present study aims to investigate the effect on residual stresses related distortion of different process parameters linked to the volumetric energy density, the scanning strategy and the specimen geometry, using the Bridge Curvature Method [4]. As reported in a previous work [46], this method had been improved and had proven to be repeatable and relevant. It should be noted that this work was focused only on determining levels of distortion, without proceeding to the calculation of the residual stresses. The results obtained were compared with those reported in the literature, in an attempt to remove the ambiguities inherent in the measurement method and the shape of the SLM part. The role of the scanning strategy was looked through the prism of the scan vector length.

2. Experimental procedure

The experimental procedure, which was fully detailed in a previous article [46], has been summarized below.

2.1. SLM experiments

Parallelepiped bridge shaped specimens, conventionally used for evaluating the residual stresses of parts in Power-Bed Fusion (PBF) processes [4,14,23,46], were produced by SLM on a ProX® DMP 200 machine (PHENIX SYSTEMS). A plasma atomized Ti–6Al–4V powder with a median diameter of about 35 µm was used. The bridge specimens, with either a rectangular or a square surface as detailed in Figure 1, were built directly on a non-preheated base plate (without supporting structures). All manufacturing experiments were performed under an argon-protective atmosphere, without contour scanning.

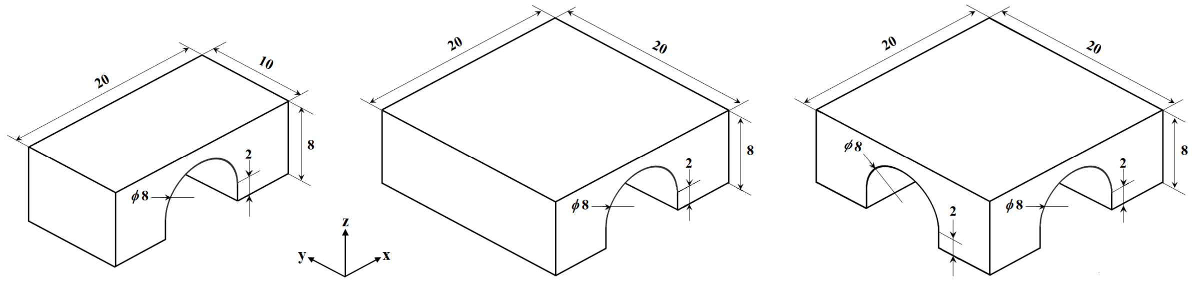

(a) **(b)** **(c)**

Fig. 1 – Geometries of the bridge specimens: **(a)** rectangular parallelepiped with a single hole, square-based parallelepiped with **(b)** a single and **(c)** double hole.

Various laser scanning strategies, described in Figure 2, were investigated on rectangular-based bridge specimens built on a same base plate. Some parameters were kept constant, such as the laser power P (300 W), the scanning speed v (1800 mm.s^{-1}), the laser spot size (70 µm), the hatch spacing (85 µm), the layer thickness (60 µm) and the number of layers (134 layers, from layer n_0 to layer n_f with f=133, to reach a height of 8 mm). Using a unidirectional back-and-forth (or zigzag) strategy, the laser scanning orientation (θ) was varied each 15° from 0 to 90° (Figs. 2a and b), the hatch angle (β) between 0 and 150° (Fig. 2c), and the scan vector length (L_v) between 2.5 and 20 mm (Fig. 2d). Concentric scanning, either inwards or outwards, was also investigated (Figs. 2e and f). The test with a scan vector length of 20 mm and θ=β=0°, which corresponds to a scanning parallel to the long side of the bridge-shaped specimen (x-axis) without change in direction from one layer to the next, will be considered hereafter as the reference test (noted Ref.). It has to be clarified that experiments performed using the alternating hatch rotation strategy with different angles β (Fig. 2c) corresponded to a variation in the orientation of the laser scanning from one layer to another between two different orientations θ=0° and β (namely layers n_0, n_2, …, n_{f-1} melted using a scanning oriented at 0°, and layers n_1, n_3, …, n_f using a scanning oriented at β). The shortening of the scan vectors was carried out by successively scanning areas of length L_v along the x-axis, which means a series of parallel stripes (for example, 2 areas of 10 mm x 10 mm for L_v=10 mm, or 8 areas of 2.5 mm x 10 mm for L_v=2.5 mm), keeping the same back and forth strategy than for the reference test.

The effect of the laser power (P) and scanning speed (v) was investigated on rectangular bridge specimens built on another base plate, using the reference scanning strategy and a layer thickness of 70 µm. Bridge specimens with a square base and either a single (Fig. 1b) or double hole (Fig. 1c) were also investigated, in order to assess the influence of the specimen shape.

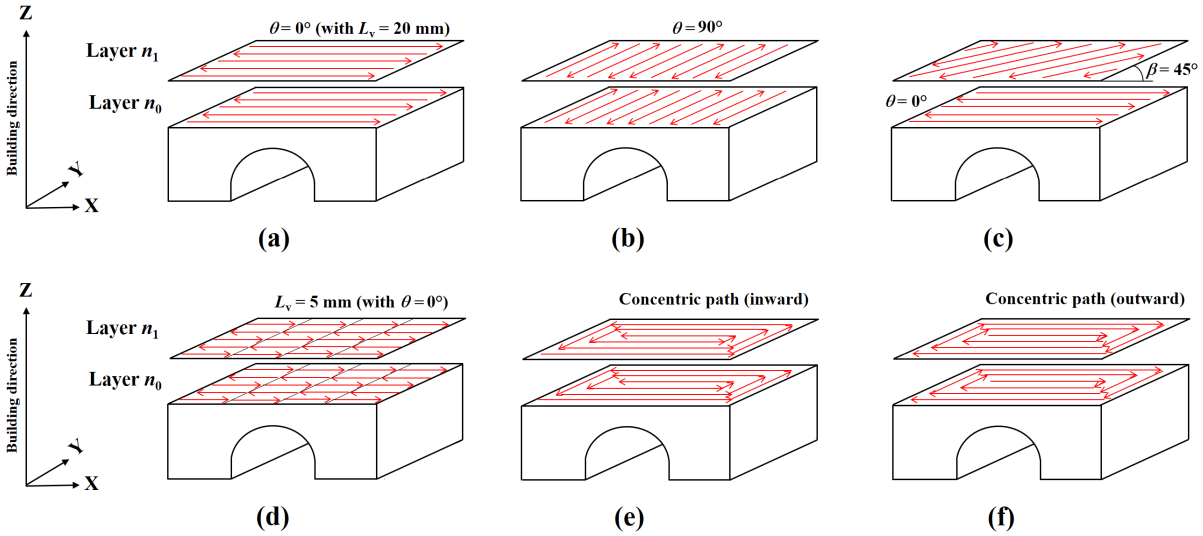

Fig. 2 – Examples of investigated laser scanning strategies: unidirectional zigzag pattern with **(a)** θ=0° (reference test) or **(b)** 90°, **(c)** hatch rotation with β=45°, **(d)** scan vectors of length reduced to L_v=5 mm ; **(e)** inwardly and **(f)** outwardly concentric scanning. (The two layers shown were sequentially repeated until reaching the last layer n_f).

For unidirectional zigzag strategies with a laser scanning orientation coinciding with the longitudinal x-axis or the y-axis of the bridge specimen, the maximum and the mean length of the scan vectors were simply considered to be equivalent to either the length or the width of the specimen. For other scanning strategies, the scan vector length could be estimated using a trigonometric approach, as represented schematically in Figure 3. In Appendix Table A1 were reported the maximum and average vector length (L_{vmax} and L_{vm}, respectively) calculated for each scanning orientation.

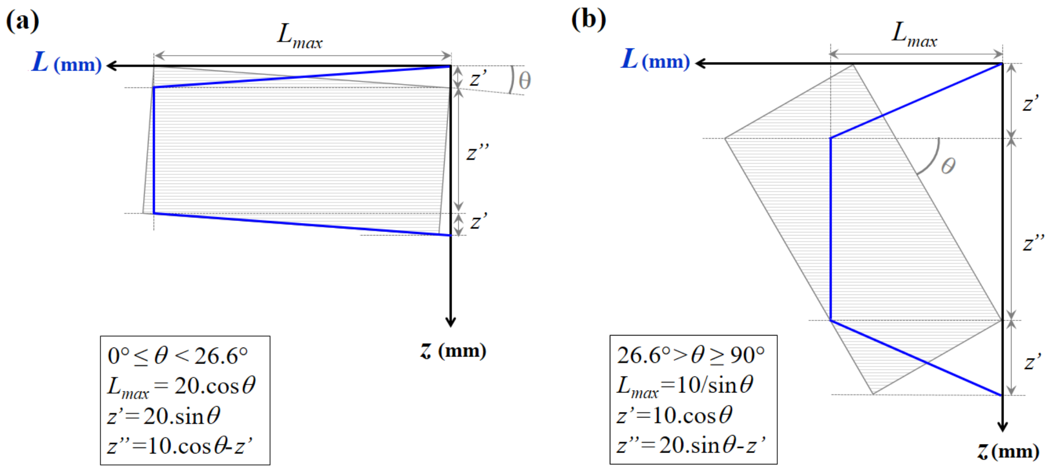

Fig. 3 – Trigonometric approach to calculate the length of the scan vectors as a function of the laser orientation θ on conventional bridge specimens: **(a)** for 0°≤θ<26.6°; **(b)** for 26.6°<θ≤ 90°.

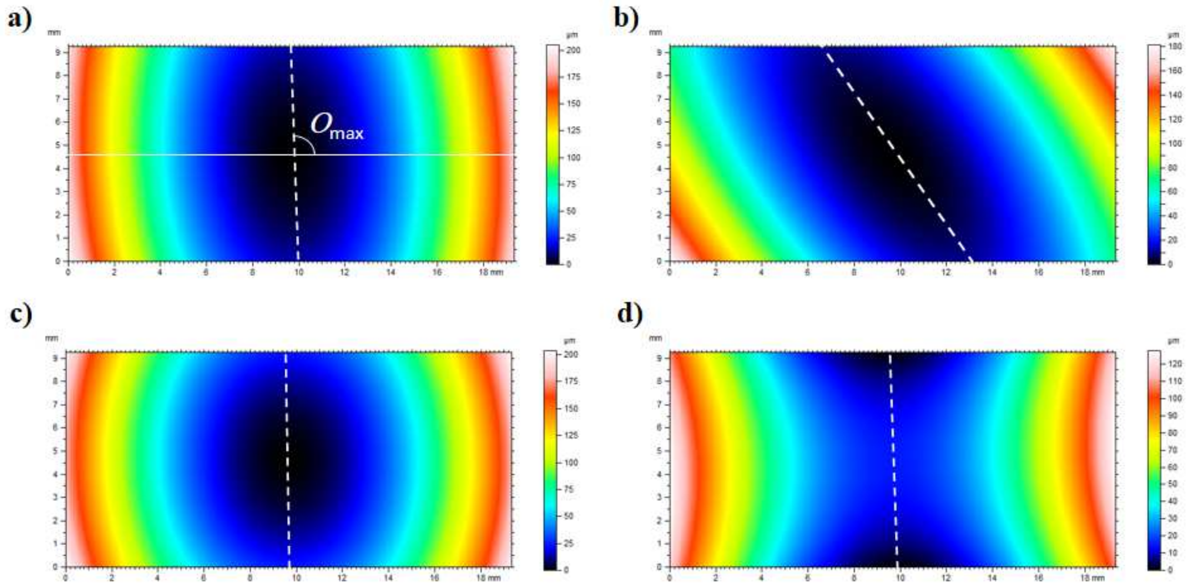

Fig. 4 – 3D polynomial distortion determined on the top surface of conventional bridge specimens built with P=300 W and v=1800 mm.s^{-1} and various strategies: **(a)** unidirectional zigzag scanning with θ=0° or **(b)** θ=45°, **(c)** inwardly or **(d)** outwardly concentric scanning [the white dotted line indicates the O_{max} orientation corresponding to the bending axis].

2.2. Distortion measurements

The bridge shaped specimens were removed from the base plate by wire Electrical Discharge Machining (EDM). It should be noted that no cracking was observed on the specimens, either before or after the separation from the base plate. Topographic measurements of the entire upper surface of the specimen were performed using an extended field confocal microscope. The distortion was extracted from 3D surface topographies using a quadratic polynomial function. Then, the distortion amplitude was quantified by standardized criteria (according to ISO 12781-1) such as the total and quadratic flatness deviation (*FLTt* and *FLTq*), respectively evaluating the peak-to-valley and root mean square amplitude on the surface. In addition, curvature attributes were determined using a Matlab® routine, especially the main curvatures (namely the maximum K_{max} and minimum K_{min} curvatures), the derived curvatures (namely the average curvature $K_m=(K_{max}+K_{min})/2$ and the Gaussian curvature $K_g=K_{min}.K_{max}$), as well as orientation of the maximum curvature (O_{max}). The orientation O_{max} describes the bending axis, which is normal to the maximum curvature plane. Graphical representations of the polynomial distortion surface are shown in Figure 4 for the most representative scanning strategies investigated here. In addition, profile (2D) measurements were also performed along both x and y-axis, for purposes of comparison with the results of the literature.

3. Results

3.1. Effect of the laser power and scanning speed

The laser power and scanning speed have a significant effect on the distortion measured in the released specimens after removing from the base plate, as reported in Appendix Table B1. The maximum flatness deviation was obtained using a middle laser power (200 W) and scanning speed (1800 mm.s^{-1}), while high power (300 W) and low speed (900 mm.s^{-1}) resulted in minimal distortion (43% less). The specimens built with a low scanning speed (<1000 mm.s^{-1}) present the lowest amplitudes of distortion (*FLTt*<180 µm). In fact, Figure 5 rather suggests that the distortion amplitude could be controlled by the volumetric energy density (E_v), which results from a combination of process parameters [8,47-48]:

$$E_v=P/(v.h.e), \qquad (1)$$

where P is the laser power (in W), v is the scanning speed (in mm.s^{-1}), h is the hatch spacing (in mm) and e is the layer thickness (in mm).

Figure 5 shows that the flatness deviation measured on the specimens decreased linearly by increasing E_v in the range [18-57 J.mm^{-3}]. Thus, increasing E_v from 18 to 57 J.m^{-1} reduced the distortion of about 50%.

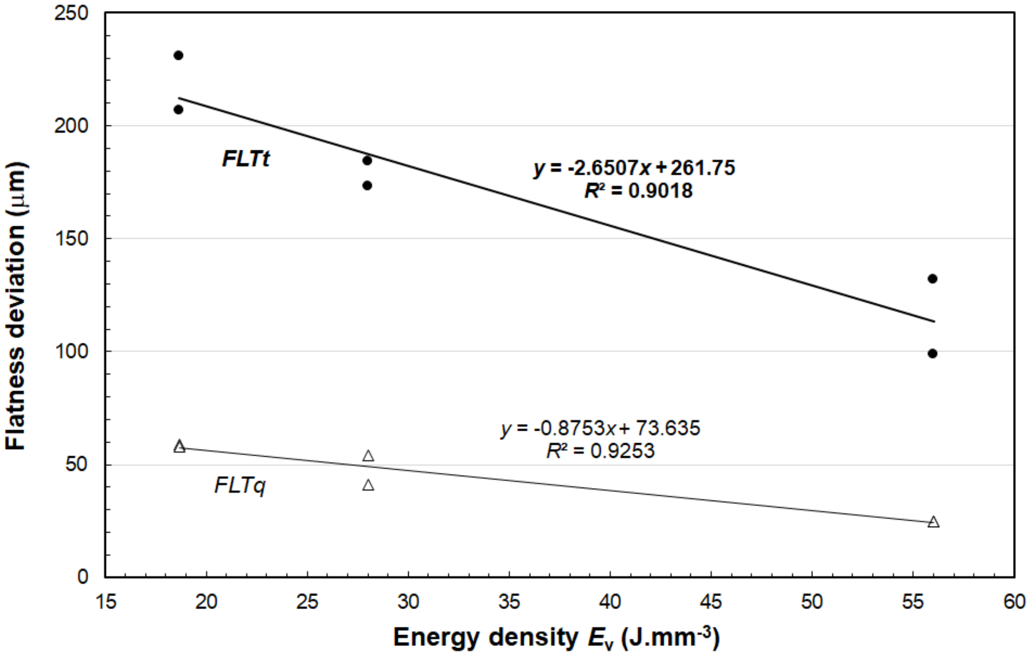

Fig. 5 – Linear relationships between the volumetric energy density E_v and the total and quadratic flatness deviations (*FLTt* and *FLTq*) measured on conventional bridge specimens.

3.2. Effect of the scanning strategy

3.2.1. Laser scanning orientation

The distortion measurements for the rectangular base bridge specimens manufactured with different laser scanning orientations θ show that both total and quadratic flatness deviations (*FLTt* and *FLTq*) decreased by increasing θ (Appendix Table B2). The reference test (θ=0°) led to the maximum distortion, while the minimum was obtained when the scan vectors were aligned with the *y*-axis (θ=90°). This corresponds to a reduction of the bending by 46% considering the *FLTt* parameter (and even 58% for *FLTq*). Such variations can be considered as significant because much higher than the dispersion shown by repeatability measurements [46].

Regarding the curvature attributes, their evolution as a function of θ was rather different. A minimum value of K_{max} was observed for $\theta \geq 60°$, while the maximum distortion corresponded again to θ=0°. A reduction of K_{max} by 26% was achieved by varying θ from 0 to 60°. In addition, a variation of the shape of the specimen bending depending on θ was highlighted in Figures 4a and b. This was accompanied with a variation of the maximum curvature orientation O_{max}, which increased steadily as θ increases. In fact, O_{max} appeared to be perpendicular to the laser scanning direction, to within 10°.

3.2.2. Hatch angle

For specimens built with various hatch angles β (consisting in alternating the scan vector directions of each two successive layers between β and 0°), the maximum distortion was found for the reference test (θ=β=0°), whatever the criterion considered (Appendix Table B3). The total and quadratic flatness deviations (*FLTt* and *FLTq*) decreased from β=0 to 90°, and then increased up to 150°. Compared to the reference test, building the specimen with a hatch angle of 90° resulted in a 55% decrease in *FLTt* and 64% in *FLTq*. The curvature attributes $K_{\max}$ and K_{m} followed overall similar evolutions versus β, with however a minimum close to 90° corresponding to a reduction of $K_{\max}$ by 26% compared to the reference test. This reduction was less (20%) for the mean curvature K_{m}, which is generally recognized as a less relevant curvature parameter than $K_{\max}$ [49]. $O_{\max}$ was, as noted above for experiments with various θ, perpendicular to the hatch angle (to within 10°).

3.2.3. Scan vector length

Compared to the reference test for which the length of the scan vectors L_{v} was maximum and equal to 20 mm, L_{v} was reduced by a factor of 2 (to 10 mm), 4 (to 5 mm) or 8 (to 2.5 mm). The results clearly indicated that the distortion decreased by decreasing L_{v}, but with a larger amplitude between 5 and 2.5 mm (Appendix Table B4). Overall, shorten the vector length by 87.5% reduced *FLTt*, *FLTq* and $K_{\max}$ values of about 44%, while the effect was lower (31%) on K_{m}. It can also be noticed that a change in the length of the scan vector had almost no effect on $O_{\max}$, which remained equal to 90° ± 3°.

3.2.4. Concentric scanning

The concentric scanning strategies gave very different amplitude distortions depending on the direction (inwards or outwards) of the laser path (Appendix Table B5). However, it can be noted that the orientation of the maximum curvature $O_{\max}$ remained close to 90° for both strategies. Compared to the reference test (with a unidirectional back-and-forth scanning), an outward concentric scanning allowed a reduction of about 38% considering *FLTt*, *FLTq* and $K_{\max}$, and even much higher (80%) considering K_{m}. In addition, the polynomial distortion showed a "saddle" (upside down) shape (Fig. 4d), completely different from the classic ellipsoidal shape generated by the other investigated strategies including the inwardly concentric scanning (Fig. 4c). This particular distortion was characterized by a negative value of $K_{\min}$ (Appendix Table B5), resulting in a negative Gaussian curvature K_{g} ($K_{\min}.K_{\max}$=-3.35

mm^{-2}). Moreover, by examining more precisely the topographic maps of the surface (Figs. 6a and b), it can be observed that the specimens built using an inwardly and outwardly concentric scanning both presented a defect in the middle of their surface.

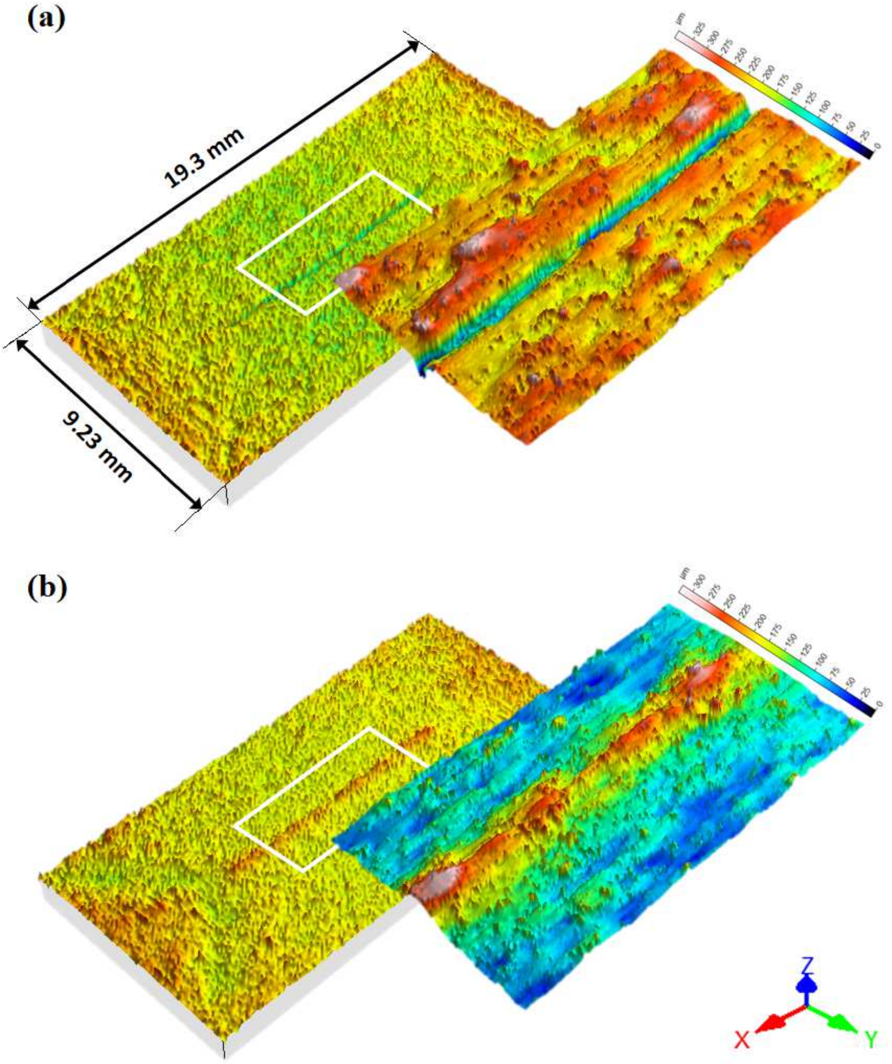

Fig. 6 – Surface height maps showing a defect of the central weld bead when the bridge specimen is built using concentric strategies: **(a)** lack of material (inward scanning direction); **(b)** swelling of the first weld bead (outward scanning direction).

3.2.5. Comparison of scanning strategies

The flatness deviation and maximum curvature achieved with different laser scanning strategies were compared in Figure 7. As can be observed, maximum distortions were achieved with either a unidirectional back-and-forth (with θ=0° and L_v=20 mm) or an inwardly concentric path. Depending on the considered criterion, the minimum flatness deviation was reached with different strategies, either the hatch rotation strategy with β=90° for the flatness deviation, or the shortest scan vectors as regards the maximum curvature.

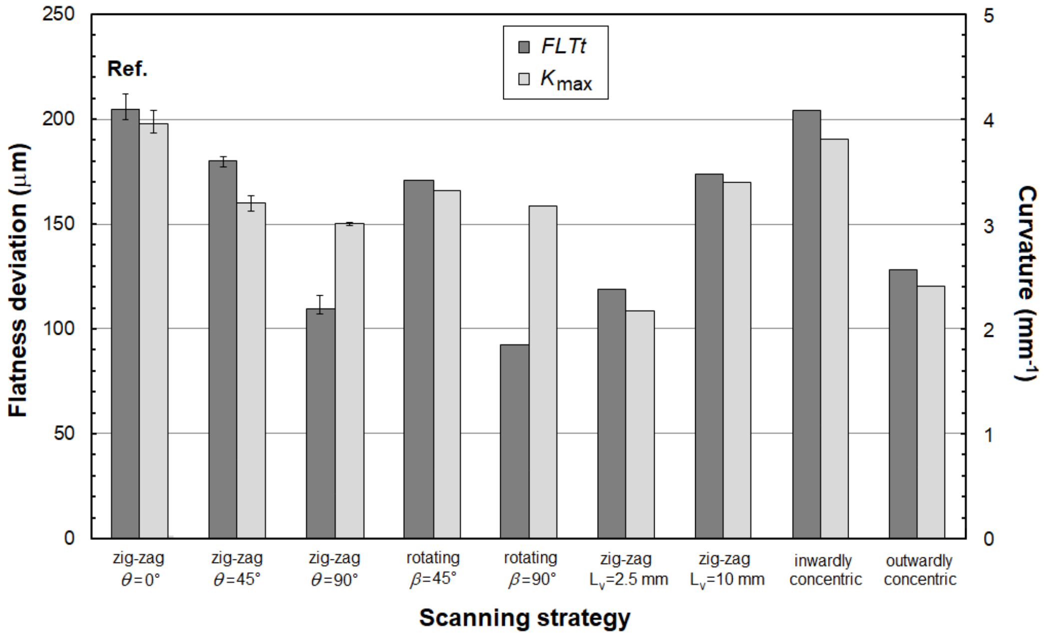

Fig. 7 – Comparison of the total flatness deviation and the maximum curvature measured on the conventional bridge specimens built with identical laser power and scanning speed (P=300 W, v=1800 mm.s^{-1}).

3.3. Effect of the specimen shape

The distortions measured on rectangular and square-based bridge specimens with single hole (built using the same volumetric energy density E_v=28 J.mm^{-3} and the reference scanning strategy) were very close, especially considering the flatness deviation and the maximum curvature K_{max} (deviation less than 1% and 3% respectively, which is negligible). On the other hand, it may be remarked that K_{min} (and therefore K_m) decreased sharply when the bridge specimen size was increased perpendicular to the scanning direction (Appendix Table B6).

The square-shaped specimen with a double-hole showed a higher distortion amplitude compared to the single-hole, especially considering the flatness deviation *FLTt* (25% higher). The main curvatures K_{max} and K_{min} were also increased (8% and 488%, respectively). In all cases, the main curvature orientation remained very close to 90°, i.e. perpendicular to the laser scanning direction.

4. Discussion

4.1. Influence of the measurement method on distortion assessment

4.1.1. Distortion criteria

In literature works related to experimental assessment of residual stresses related distortion by the Bridge Curvature Method [4,12,14], authors considered a 2D approach (often measuring the deflection angle along the *x*-axis of the specimen - sometimes also along the *y*-axis - to estimate the specimen distortion, although it is sometimes based on the acquisition of surface topographies). In this work, the approach was somewhat different because the distortion was quantified using 3D parameters (such as the total flatness deviation *FLTt* or the maximum curvature $K_{\max}$) determined on the upper surface of the specimen [46]. As the distortion is strongly directed along the scanning direction, the values of $K_{\min}$ were often relatively low and less discriminating than $K_{\max}$. The analysis of the effect of the process parameters on the specimen curvature will therefore preferentially be based on $K_{\max}$ and $O_{\max}$.

Results regarding the effect of process parameters are broadly in agreement with those reported in the literature for similar SLM experiments and geometry of bridge specimens, since the same trends were observed. However, their interpretation may differ considering the measured distortion values. For example, Kruth et al. [4] found that the curling angle α (measured at the bottom of the two pillars previously cut from the base plate by wire EDM) was reduced by only 13% using ten times shorter scan vectors (2 mm instead of 20 mm). In comparison, the results of the present study indicated a greater reduction (47% considering either *FLTt* or $K_{\max}$). On the other hand, they found a reduction of 59% of α when the vectors were oriented at θ=90° instead of 0°, while we observed a smaller reduction (46.4% for *FLTt*).

In order to better evaluate the differences in the results given by the two methods, the curling angles α reported in [4] were converted into equivalent distortion amplitudes (considering a V-shaped distortion and extrapolating the curling of the pillars on the upper surface). The converted results were compared to the profiles extracted along the *x*-axis on the top surface of specimens investigated in the present study. In Figure 8a was plotted the evolution of the distortion amplitude as a function of the scan vector length L_v (using a unidirectional zigzag scanning with θ=0°). The two curves showed the same trend with however higher values (up to 40% higher) for data from Kruth et al. [4]. The same comparison was made for specimens built with different laser orientations θ, and again, despite a similar trend of both curves, data from Kruth et al. were characterized by significantly higher values (Fig. 8b). It should be specified that the BCM method was described as "qualitative" by these authors. However, the 3D approach proposed here provided more information with more precision.

As can be seen in Figure 9a, the evolution of the distortion amplitude as a function of L_v was slightly different depending on whether *FLTt* or K_{max} was considered. An enhanced effect of decreasing the length of the scan vector from 5 to 2.5 mm - and to a lesser extent from 20 to 10 mm - can be noted, while the curve in Figure 8a showed a smaller range of variation and a clear asymptote beyond L_v=10 mm. Different trends versus θ were similarly observed according to the measurement method (Fig. 8b vs. Fig. 9b), thus confirming the importance of the criterion selection in the interpretation of the results. But in addition, whereas *FLTt* and K_{max} followed a close and parallel increase as L_v increased, these two parameters varied quite differently depending on θ. The decrease of *FLTt* as a function of θ could be approximated by two straight lines with different slopes and a transition to θ=45°, while K_{max} followed a sharp decrease and then stabilized at a minimum value beyond 60°. This angle corresponded to a stabilization of the scan vector length around 10 mm (Appendix Table A1). Such differences could be explained by a greater sensitivity of flatness deviation parameters to the distance over which the deformation was evaluated, and therefore to the specimen shape.

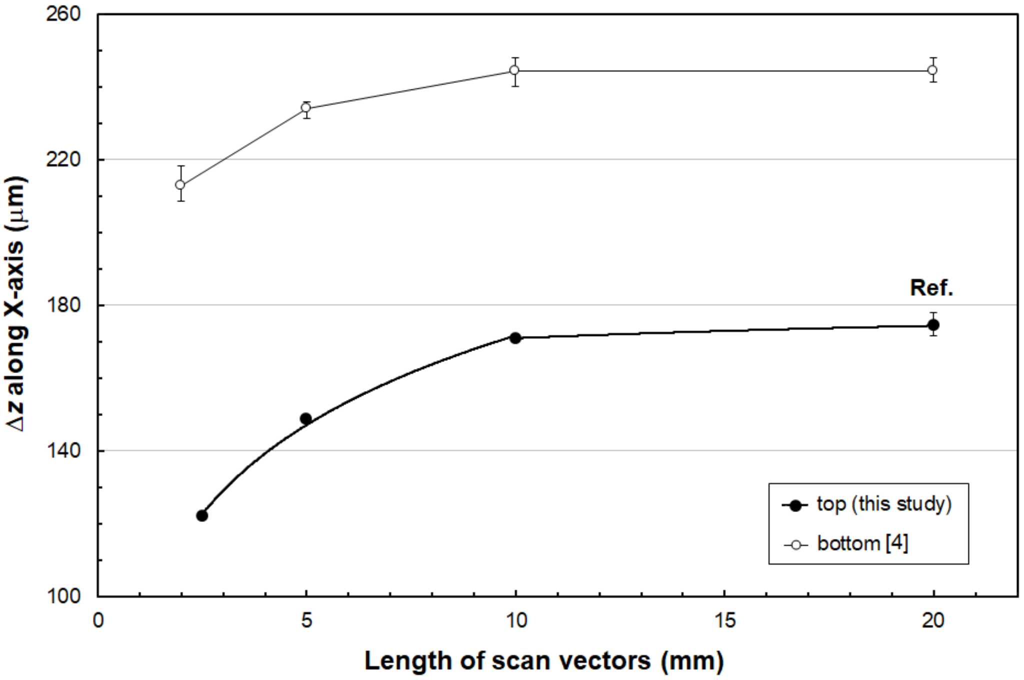

(a)

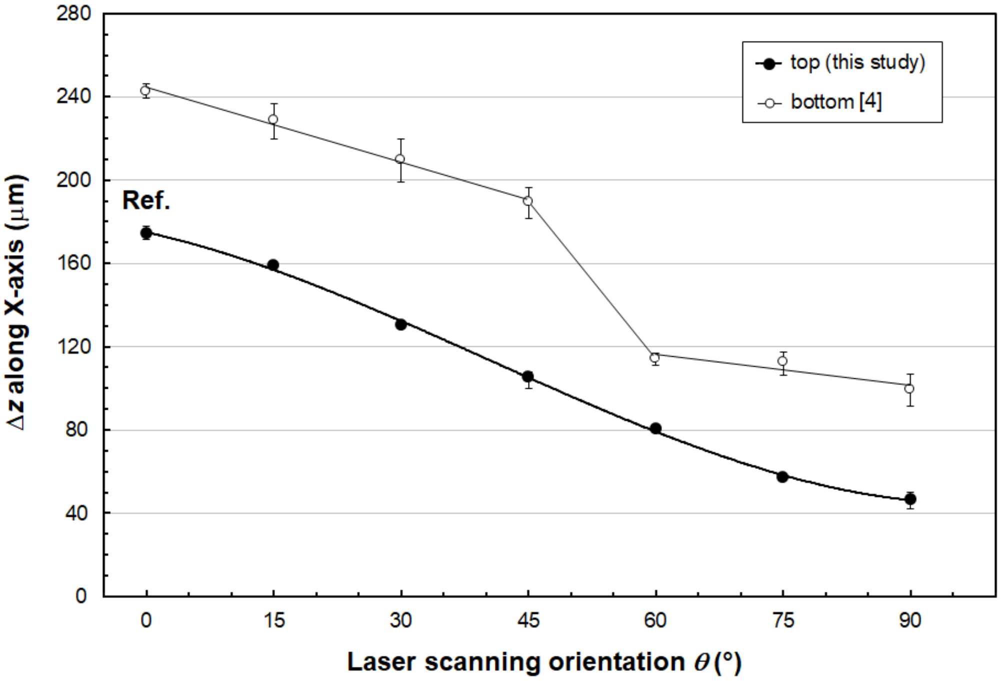

(b)

Fig. 8 – Effect of **(a)** the scan vector length L_v and **(b)** laser scanning orientation θ on the distortion amplitude Δz along x-axis of conventional bridge specimens built with a unidirectional back-and-forth scanning: comparison with the results of Kruth et al. [4].

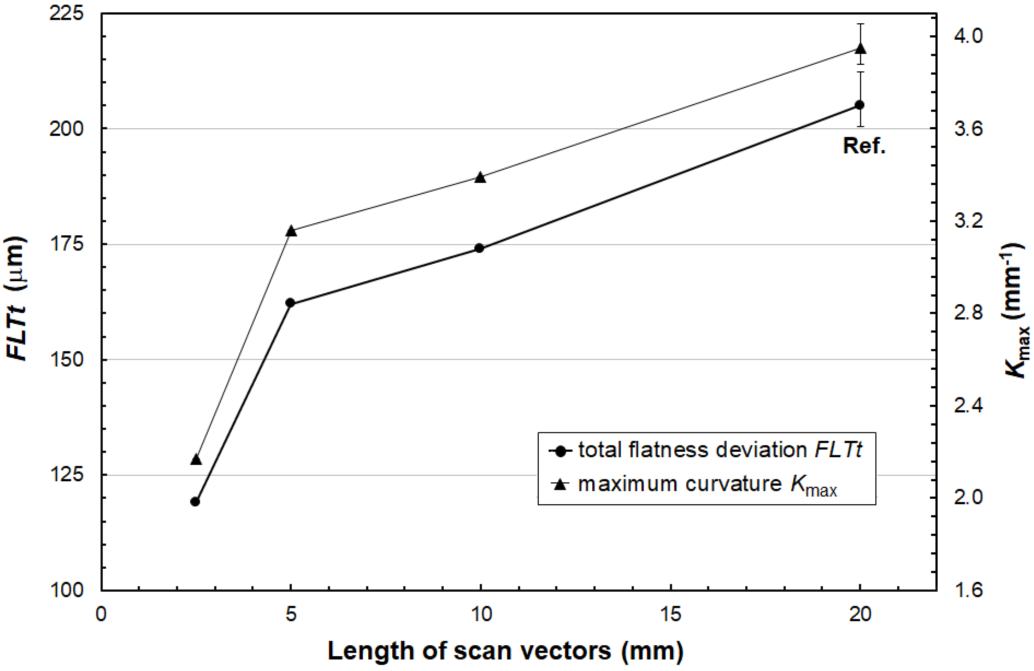

(a)

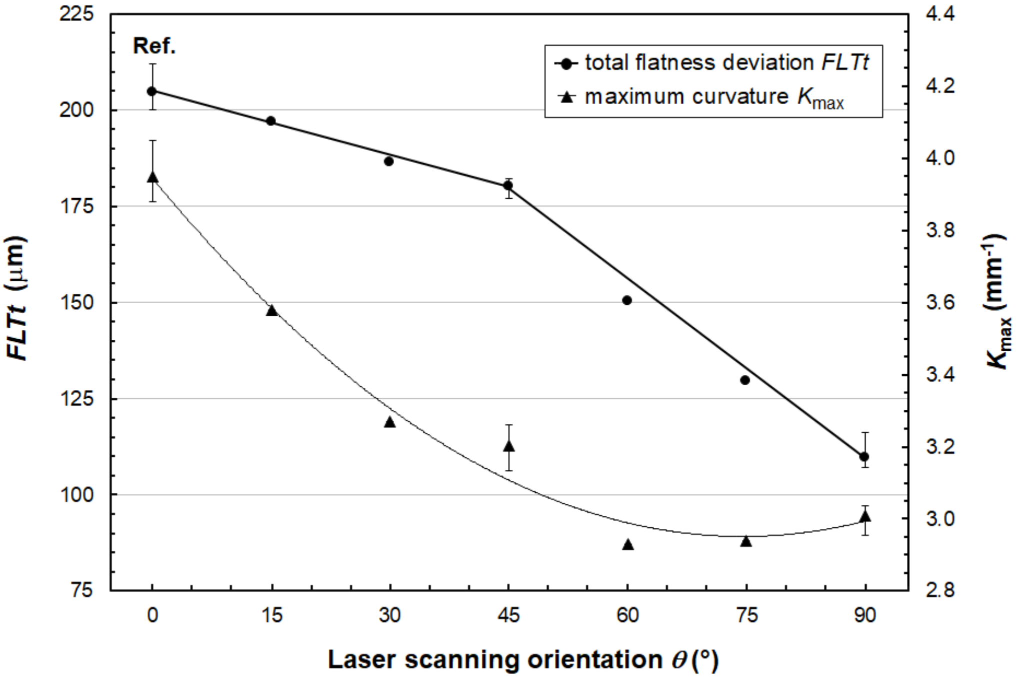

(b)

Fig. 9 – Effect of **(a)** the scan vector length L_v and **(b)** laser scanning orientation θ on the distortion amplitude determined on conventional bridge specimens by the total flatness deviation (*FLTt*) and the maximum curvature (K_{max}).

In several studies [18,50-51] aiming to validate numerical simulation models of residual stresses, a difference between simulated and experimental data was observed and often attributed to a lack of refinement of the model. Since the accuracy of the estimate of residual stresses is inherently dependent on the accuracy of deformation measurements, we believe that this difference could be linked – at least in part – to overestimated experimental data due to a measurement artefact from 2D evaluation. Indeed, such a method always involved measuring the bending of the base and the upper surfaces of the bridge along the *x*-axis, whatever the scanning orientation. Furthermore, and as previously discussed in [46], measuring the distortion on the pillars after separation of the support plate could further introduce errors linked to the cutting and the lack of precision of the angle measurement (low values). This hypothesis was supported by recent work of Mishurova et al. [14] investigating the effect of the energy density on residual stresses determined experimentally on the same geometry of bridge specimens. In their experimental investigation, these authors measured the "deflection angle" (otherwise equivalent to half the "curling angle" used in [4]), both on the pillar bottom and on the top surface of their specimens. They noted that the deflection angle was slightly lower when determined on the upper surface than on the bottom facets. This gap could also be related to the difference of released residual stress fields developed in the specimen, which differed along the building direction (z-axis).

The effect of the laser scanning orientation θ on the flatness deviation measured on the specimen was previously highlighted for a unidirectional back-and-forth scanning, with θ ranging between 0 and 90° (Fig. 9b). In Figure 10 were also plotted the data corresponding to a variation of the hatch angle β as a function of the square sinus of the orientation ($\sin^2(\beta)$), in order to take into account the symmetry with respect to 90° induced by the specimen geometry (for example, a scanning oriented at 105° should thus be equivalent to a scanning at 75°). As can be seen, all the data were fitted on the same polynomial curve, with a strong determination coefficient (R^2>0.95). In the literature, hatch rotation strategies have been reported to reduce anisotropy, leading to a more or less pronounced impact on the density, microstructure, tensile strength and residual stresses of SLM parts [4,3,52-55]. Several experimental and numerical studies have indeed shown (in agreement with Figure 10) that the larger the angle between two successive layers, the lower the residual stresses [4,8-9]. According to Robinson et al. [56], the effect on the magnitude of residual stresses of hatch rotation other than alternating 90° was however unclear, and the directionality of the stress state would depend on the geometry (aspect ratio) of the part. This hypothesis was supported by the present study, which clearly indicated that equivalent reduction in distortion was obtained by increasing the orientation θ of the vectors using a unidirectional back-and-forth scanning, and that this reduction would rather be due to a shortening of the scan vectors induced by the laser scanning rotation rather than to the hatch rotation strategy. In addition, the effect of the scanning orientation being the same with or without alternated rotation at 0° between two successive layers (Fig. 10), we can assume that the last layer would have a predominant effect on the distortion of the upper surface. In fact, specimens built with a hatch rotation presented 67 layers according to the direction 0° and 67 layers (including the last one) oriented to β, while specimens built with a single orientation had 134 layers lased along θ. Many experimental and numerical studies [2,13,16,29-30,36,57-58] have indeed revealed that the maximum tensile residual stresses were in the last layer of the part (or at least close to the top surface).

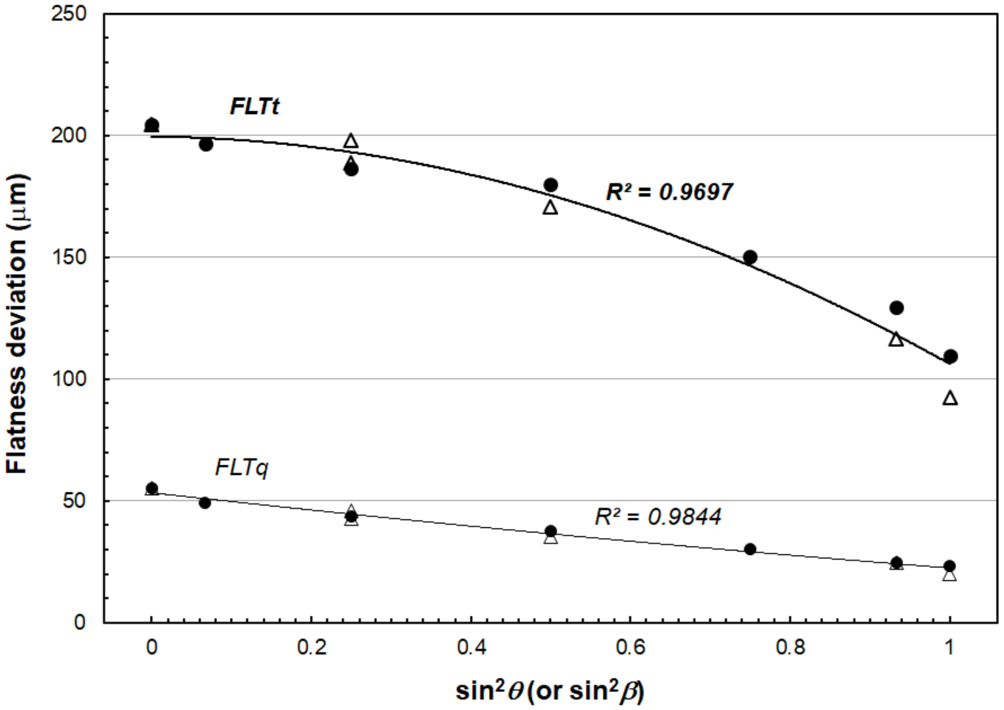

Fig. 10 – Relationship between the flatness deviation and the orientation of the scan vectors, for conventional bridge specimens built with the same process parameters (P=300 W, v=1800 mm.s^{-1}). [Black markers represent the data resulting from a unidirectional back-and-forth scanning strategy (θ), and white markers the data resulting from a hatch rotation strategy (β)].

4.1.2. Stress state anisotropy

The measurement method used in this study also allowed, by determining the curvature parameters of the specimen, to access the orientation $O_{\max}$ of the main curvature $K_{\max}$. An effect of the laser scanning orientation θ on $O_{\max}$ was previously mentioned (Section 3.2.1). Figure 11, gathering all the experiments carried out using a same volumetric energy density (E_v=32.7 J.mm^{-3}), confirmed that $O_{\max}$ was related to the main orientation of the scan vectors by a linear law. For inwardly and outwardly concentric scanning and due to the shape of the specimen, it can be assumed that the main orientation of the scan vectors was 0° (because 75% of the surface was scanned along x-axis while 25% was scanned along y- axis). The equation indicated a slope very close to 1 and a y-intercept close to 90° (within 2°), clearly stating that the orientation of the bending axis of the upper surface was perpendicular to the scan orientation. It should also be noted that the coefficient of determination of the data fit was remarkably high (R^2=0.987), again attesting to the reliability and good repeatability of the measurement method (coefficient of variation <1% for $O_{\max}$) as demonstrated in [46]. As previously observed for the distortion magnitude, it seems that the orientation of the deflection ($O_{\max}$) would also be mainly controlled by the scanning strategy of the last layer.

As pointed out by Robinson et al. [27,56], the main direction of the residual stress with respect to the scanning orientation has been much debated in the literature, with contradictory assertions depending on the authors. Our findings, based on a full 3D characterization of the surface distortion, allowed to state unambiguously that the greatest stress is generated parallel to the scanning orientation, in agreement with the most recent studies [3-5,13,21,27-28,56,59].

However, it can be noticed in Table B1 (Appendix) that for experiments with a low scanning speed (v<1000 mm.s^{-1}), the orientation of the main curvature O_{max} was not perfectly orthogonal to the scanning orientation ($O_{\text{max}} \neq 90°$). In fact, Figure 12 revealed that a power law related the deviation (O_{max} -90°) to v: the more v decreased, the more the maximum curvature became parallel to the scanning direction (O_{max} -90° tended to 90°, when it should be equal or very close to 0° as previously stated by Figure 11). In addition, the laser power (P) seemed to have no effect for high scanning speeds (data points with v=1800 mm.s^{-1} and two different P almost overlapped), while for a low v, the higher the power, the greater the deviation (data points with v=600 mm.s^{-1} and two different P were indeed far apart on the curve). This could be explained by the thermal gradients induced by scanning speed and the melt pool dimensions. For high scanning speeds, the stress state was strongly anisotropic and independent of the laser power. In fact, thermal gradients are much more sensitive to the scanning speed. At low speed, the thermal gradients (and therefore the stresses) decrease along the scanning direction, thus reducing the anisotropy of the stress state, which could explain the deviation from the normal observed for O_{max}. Under these conditions, the laser power slightly impacts the stress amplitude because it widens the melt due to the increase in the deposited energy [3]. This was supported by the surface topography maps inserted in Figure 12, which clearly showed that specimens produced with the lowest scanning speed had the coarsest surface textures, with large amplitude defects reflecting a large melt pool in all directions (and the higher the power, the larger the melt pool, hence the difference between the surfaces S1 and S2). By comparison, specimens built with a higher scanning speed had a finer texture, reflecting an elongation of the melt pool (and the higher the speed, the thinner the melt pool, hence the difference between surfaces S4 and S5).

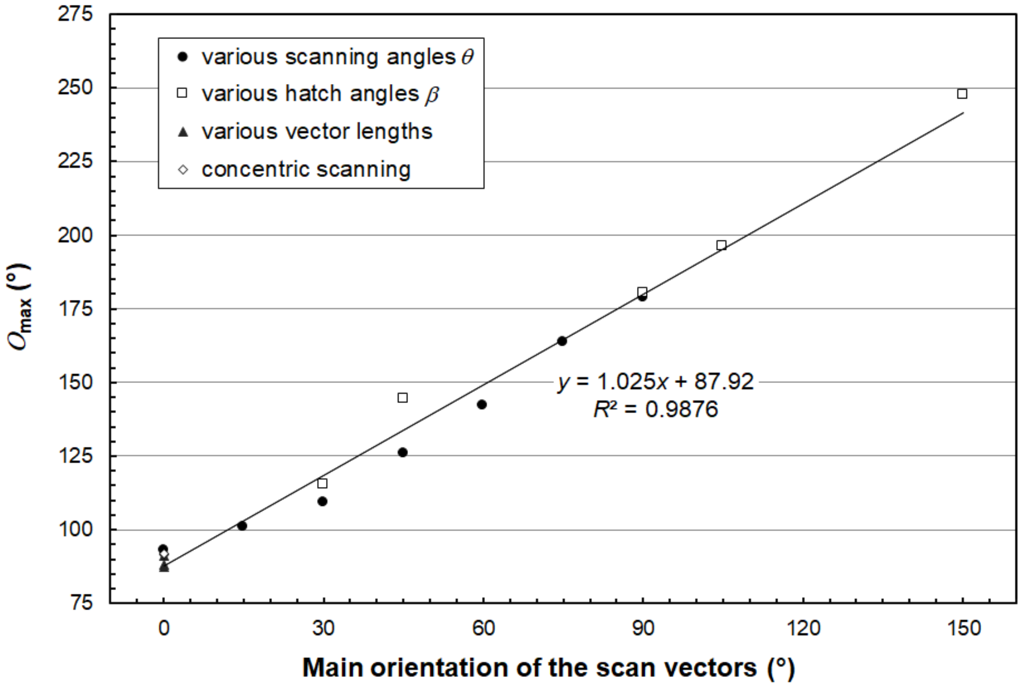

Fig. 11 – Linear relationship between the orientation O_{max} of the maximum curvature and the main orientation of the scan vectors, for all conventional bridge specimens built with the same process parameters (P=300 W, v=1800 mm.s^{-1}).

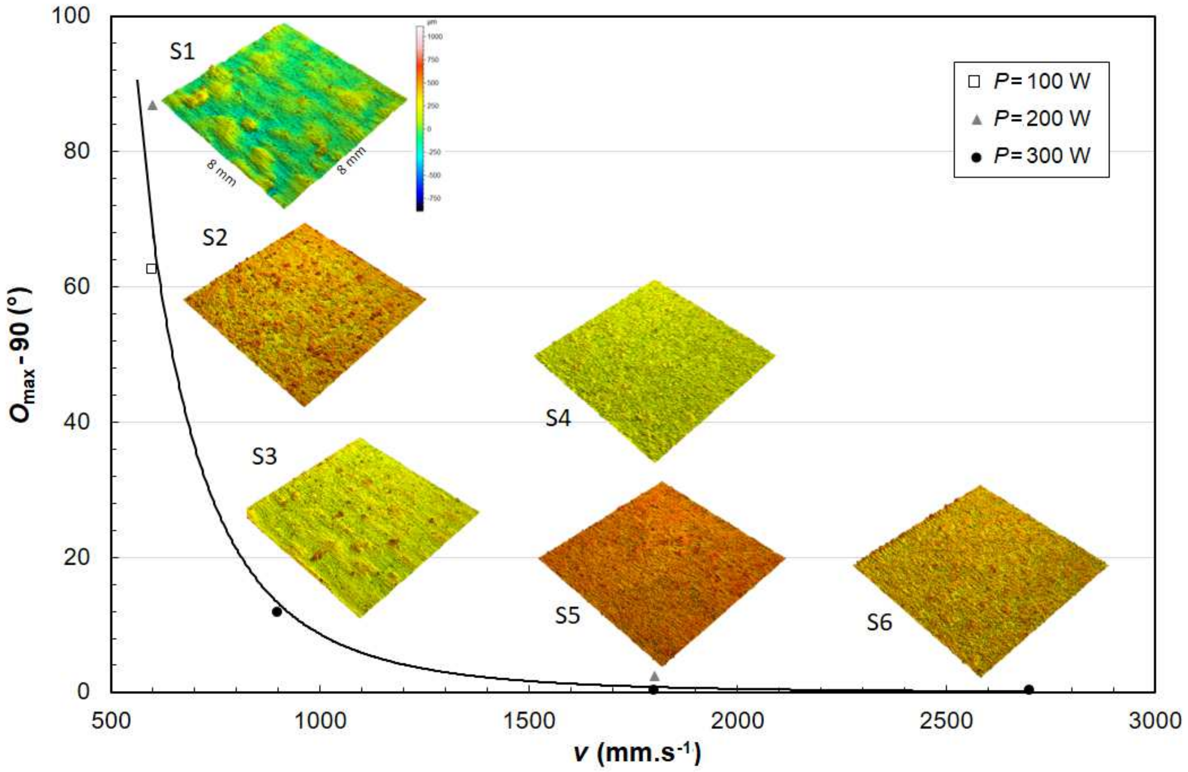

Fig. 12 – Evolution of the deviation from the normal orientation (O_{max}-90°) of the maximum curvature measured on conventional bridge specimens with the scanning speed v and the laser power P (surface topography maps are displayed near each data point to illustrate the surface texture and dimensions of the melt pool).

4.1.3. Specimen geometry

Experiments using different shapes of bridge specimens showed that the geometry had an effect on the part distortion (Section 3.3). This is consistent with literature works, which reported very different distortion magnitude depending on the specimen shape and size (bridge specimens versus cantilever specimens for example [3]). For a same scanning orientation, doubling the surface of the specimen (rectangular versus square shape) did not change the flatness deviation *FLTt*, neither the maximum curvature $K_{\max}$. It must be emphasized that, in both cases, the scanning orientation was perpendicular to the hole axis, i.e. in the direction favoring the distortion.

In contrast, adding a second hole along x-axis led to increase significantly the distortion in both directions (x and y), and especially in the transversal directions (6 times higher than with a single hole). The second hole promoted the release of the transverse residual stresses (corresponding to $K_{\min}$) by decreasing the stiffness (area moment of inertia) along y-axis.

The dissymmetry of the mechanical loading during the release of residual stresses along x and y is inherent to the geometrical asymmetry of the single hole bridge specimens, especially with a rectangular-based shape. This was illustrated in Figure 13 representing the distortion magnitude along the orientation of the main curvatures ($K_{\max}$ and $K_{\min}$) versus the orientation of the laser scanning orientation θ. It must be observed that the two curves were not symmetrical neither in amplitude, nor in angle. The maximum magnitude was much higher for θ=0° than 90° because of the presence of a hole only along y-axis. Otherwise, the rectangular shape involved different lengths of scan vectors depending on θ, which could explain in part the decrease in distortion magnitude. The deflexion Δz along $O_{\max}$ started to increase from 45° and reached its maximum at 75°, while it decreased from 30° to stabilize from 60° along the perpendicular direction (corresponding to $K_{\max}$). For symmetrical shapes, these curves should have crossed around 45°. To avoid any ambiguity, it would therefore be preferable to use axi-symmetric geometry that does not favor any particular direction and simplify the analysis of results. On the other hand, it is also necessary that the specimen geometry induces large deformation amplitudes during the relaxation of residual stresses, so as to exceed the resolution limit inherent to each measurement method (estimated for the present study to 40 µm [46]). From this point of view, square based double-bridge could be an interesting alternative to conventional bridge specimens, although the square shape was not really axisymmetric. Some tests were performed on cylindrical shaped specimen with a flat surface and a hemispherical hollow, but this geometry did not give rise to distortions of sufficient amplitude so that the results could be interpreted without great measurement uncertainty.

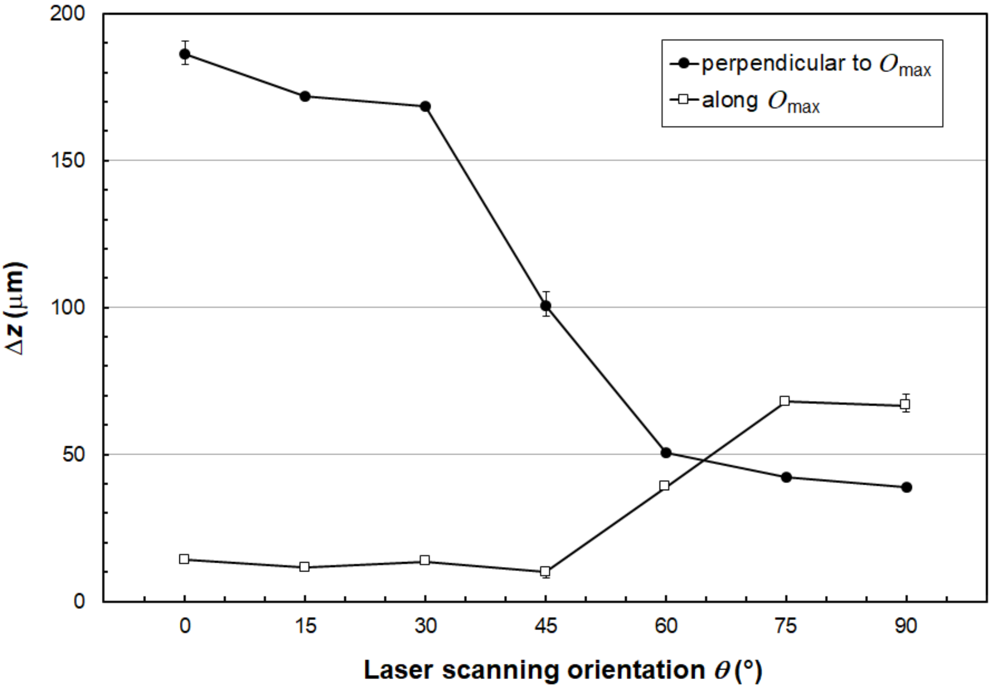

Fig. 13 – Distortion amplitude Δz measured along and perpendicular to O_{max} versus the laser scanning orientation θ.

4.2. Effect of process parameters

4.2.1. Energy density

Several recent studies have demonstrated a connection between residual stresses and the volumetric energy density E_v (as defined in Equation (1)). Experimental data from the present study and other literature works [4,12] have been plotted in the same graph (Fig. 14), initially established by Mishurova et al. [14]. It is noticeable that overall, the distortion was strongly dependent of E_v below a critical level beyond which it stabilized to a minimum value. For low E_v values (<100 J.mm^{-3}), linear relationships were established, with a slope decreasing by increasing the preheating temperature of the base plate. The results of the present study (with no preheating and using a same unidirectional zigzag scanning strategy) were close to those of Malý et al. [12] with a low preheating temperature. The gap between the two straight lines could be linked to the difference in the scanning strategy parameters on the one hand, and the measurement accuracy on the other hand. Moreover, it can be observed that data from Malý et al. [12] were also widely scattered around their respective correlation lines.

Otherwise, data from Kruth et al. [4] appeared again well above the range of values found in other studies, confirming their likely over-estimate. The large scattering of data obtained with a same energy density was induced in particular by a change in the length of the scan vectors, as also noticed for the results of the present study. The volumetric energy density does not take into account neither the energy introduced by subsequent passes of the laser as successive powder layers were deposited and melted, nor the material properties [47,60]. In addition, it does not consider other process parameters such as the preheating of the base plate and the scanning strategy. It is therefore not sufficient alone to predict the residual stresses and resulting distortions during manufacture of the part, even if it is widely used to optimize SLM parameters and produce dense parts [8,11,47,61].

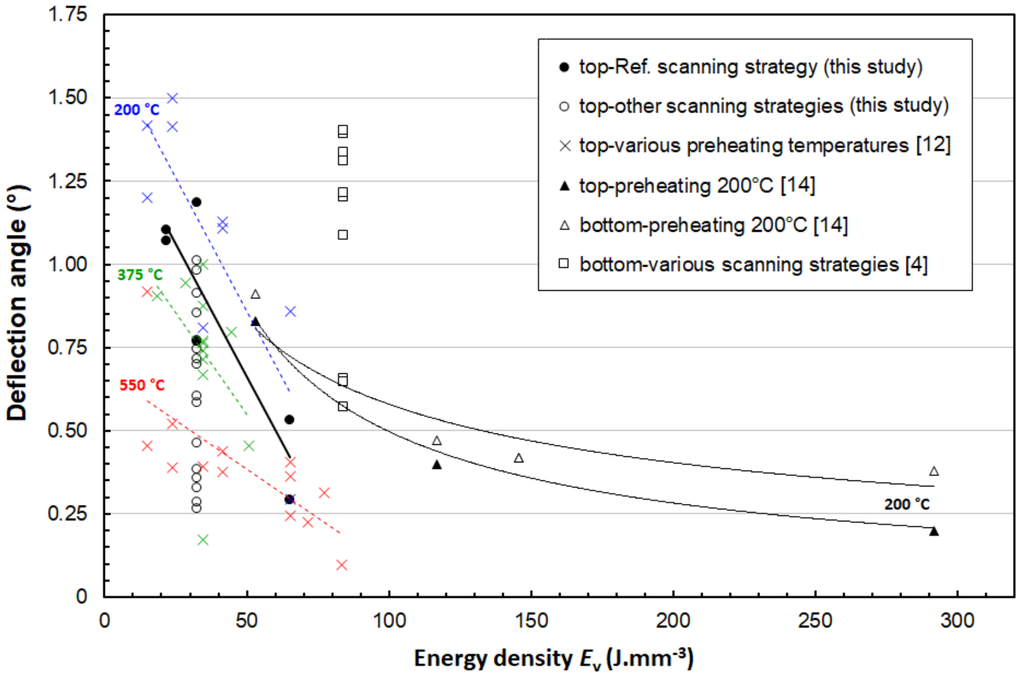

Fig. 14 – Effect of the volumetric energy density E_v on the deflection angle (used to assess the distortion amplitude): experimental data from the present study and data found in literature works (Kruth et al [4], Malý et al [12], Mishurova et al [14]). The temperature indications refer to a preheating of the baseplate.

4.2.2. Length of scan vectors

It has been shown previously that the specimen deformation increased continuously by increasing the length of scan vectors from 2.5 to 20 mm, using a unidirectional back-and-forth scanning (Fig. 9a). Such a relationship between the residual stresses and the length of the scanning track has been highlighted in numerous experimental or modelling works [2-4,8,10,15,17-18,25,51,59,62-63], through various kinds of scanning strategies (zigzag, island, chessboard or fractal types). In particular, Ali et al. [25] showed that for the chessboard strategy, increasing the size of the sub-sectors resulted in an increase in residual stress.

Changing the laser orientation θ necessarily induced a change of the scan vector lengths, as indicated in Table A1 (Appendix) revealing a broad variation of the maximum and mean lengths of the vectors L_{vmax} and L_{vm} (roughly between 10 and 20 mm) depending on θ. In addition, the relative orientation of the scanning with respect to the hole axis of the bridge specimen changed with θ. This had a direct impact on the distortion, which was superimposed on the effects of shortening of the length of the scan vector. In the following, the effect of the different scanning strategies will be analyzed through the vector length.

In Figure 15, the linear distortion amplitude Δz according to K_{max} has been reported as a function of L_{vmax}, for different strategies and a constant E_{v}. The data could be fitted by two different curves, both showing an increasing trend as L_{vmax} increased. The first one corresponds to data obtained by a scanning perpendicular to the bridge hole axis (θ=0°), and the second one to other scanning orientations. This difference could be due to geometrical effects and, as discussed in Section 4.1.2, the scanning strategy should consider the geometry and orientation of the part. An exception was however noted for the outwardly concentric scanning, which resulted in much less distortion than the inwardly concentric scanning. Although both cases led to a similar vector length, the induced thermal gradients and therefore residual stresses were different, as revealed by simulation works [64]. In addition, the outwardly concentric path was previously described as a special case, due to the "saddle" shape of the polynomial distortion (Fig. 4d) and a swelling of the central weld bead (Fig. 6b).

By considering now the evolution of *FLTt* as a function of the mean length L_{vm} as plotted in Figure 16, it can be remarked that when the scanning orientation was less or equal to 45°, all the experimental data gathered on the same power law curve (except again for the outward concentric scanning). In contrast, *FLTt* could vary considerably – despite very close L_{vm} values (~ 9 mm) – when the orientation of the vectors was greater than 45°. In fact, the closer the scanning direction was to 90°, the smaller the flatness deviation. Approaching 90°, the scanning became parallel to the hole axis of the bridge, and thus the residual stresses were released along the stiffer side of the specimen. As explained previously, the use of axisymmetric specimens would induce the same mechanical loading (bending condition) as well as vector length whatever θ.

In order to avoid the effect of the specimen dimension, the maximum curvature could be considered, as illustrated in Figure 17 showing the effect of L_{vm} on K_{max}. A single power law curve quite well gathered all the experimental points, except again the outward concentric scanning. In fact, K_{max} takes into account the main orientation O_{max} of the deformation (which was directly linked to the scanning orientation) as well as the length of the scan vector, while limiting the effect of the geometry.

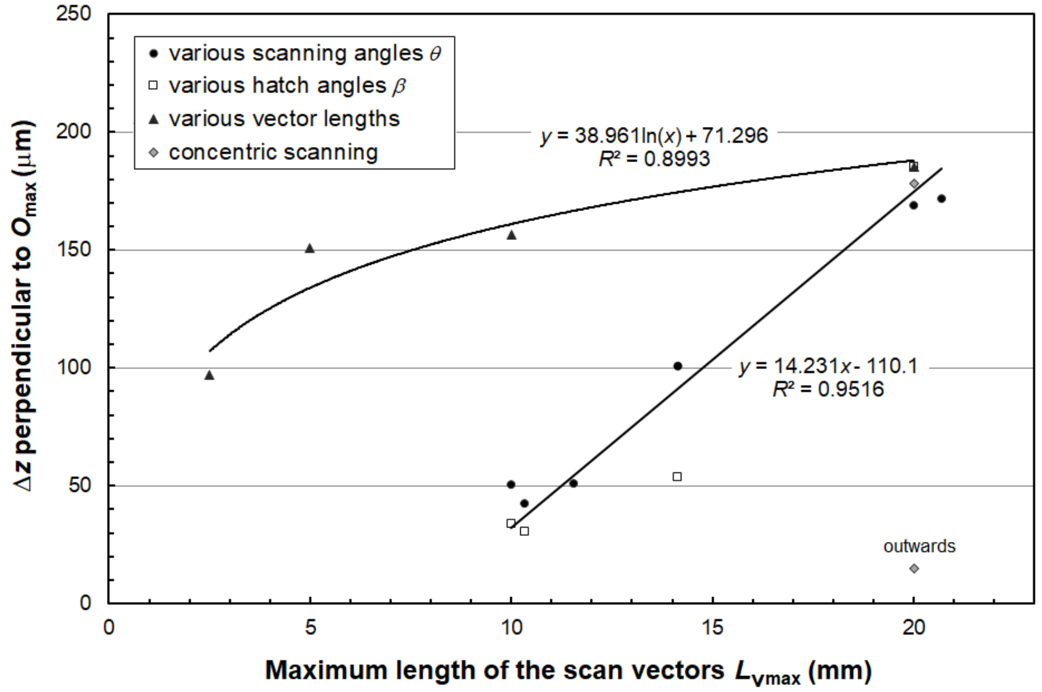

Fig. 15 – Evolution of the distortion amplitude Δ*z* measured perpendicular to O_{max} as a function of the maximum length of the scan vectors L_{vmax}, for conventional bridge specimens built with the same energy density (E_v=32.7 J.mm^{-3}) and various scanning strategies.

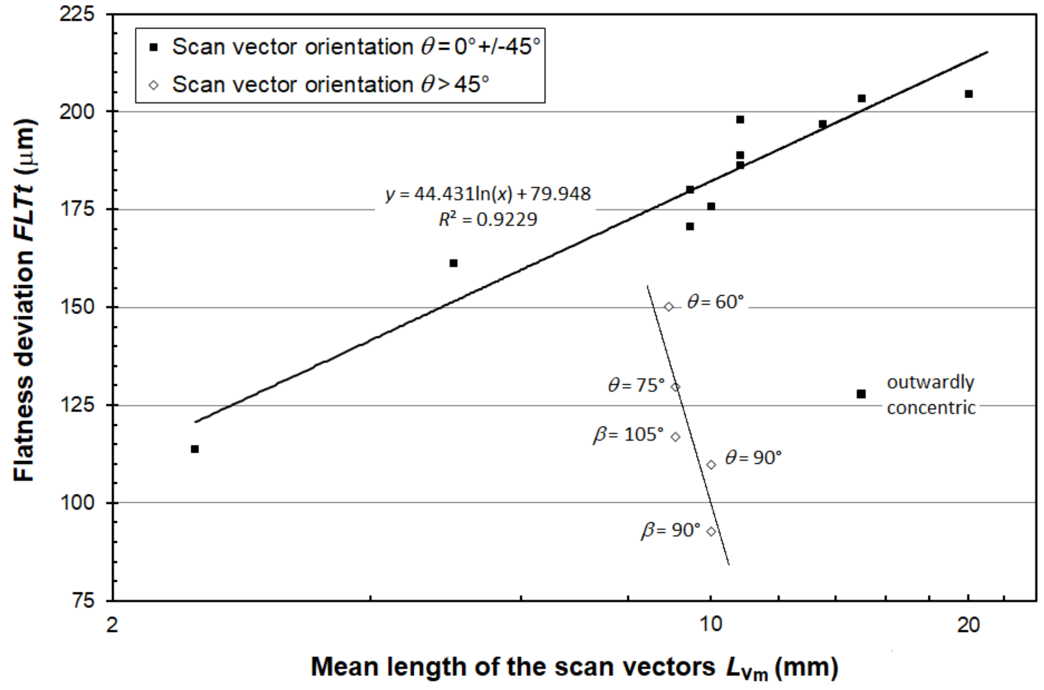

Fig. 16 – Evolution of the total flatness deviation *FLTt* as a function of the mean length L_{vm} of scan vectors, for conventional bridge specimens built with the same energy density (E_v=32.7 J.mm^{-3}) and various scanning strategies.

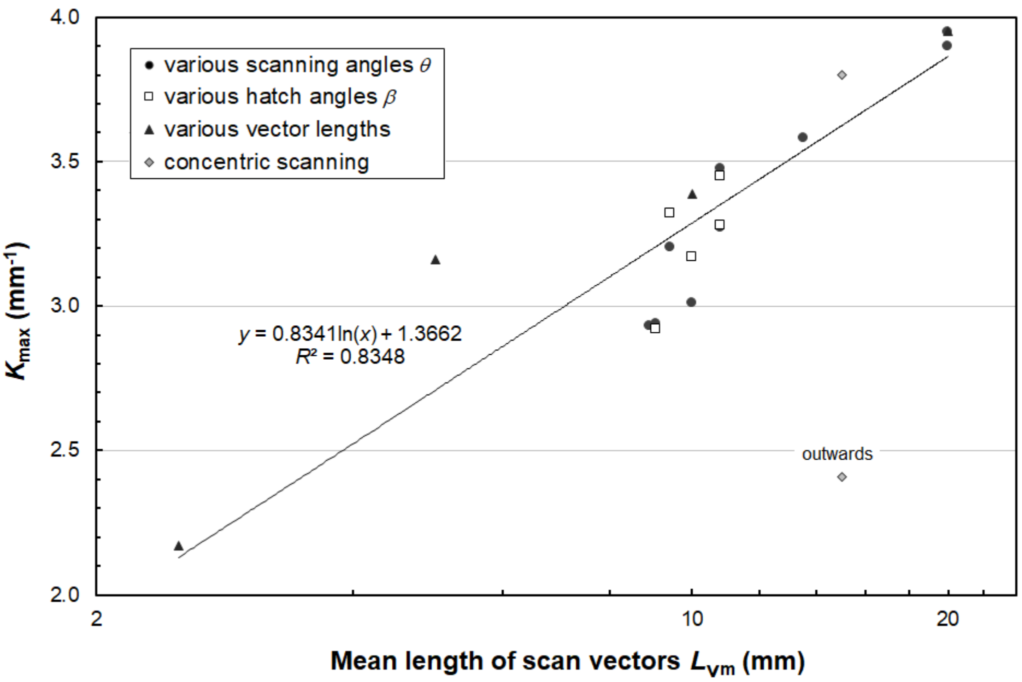

Fig. 17 – Evolution of the maximum curvature K_{max} as a function of the mean length L_{vm} of scan vectors, for all conventional bridge specimens built with the same energy density (E_v=32.7 J.mm^{-3}) and various scanning strategies.

4.3. Guidelines for a new analytical modelling approach

The volumetric energy density E_v, which is considered as an engineering parameter, includes the effect of energetic process parameters (v, P, h, e) on residual stresses. E_v describes the average energy per volume of material [8], but does not take into account the length of scan vectors that also influences the thermal gradients and cooling rates. Indeed, using shorter vectors decreases the cool down time between two adjacent deposited tracks, leading to reduce the thermal gradients [3]. This is the reason why the island or chessboard scanning strategies, which consists of dividing the area to be scanned into small square islands with a rotation of the scanning from one sector to another, generates lower residual stresses compared to the zigzag pattern [4,17,19-20]. On the same idea, these strategies can be optimized by choosing the scanning sequence to obtain a more uniform heating of the powder bed in order to reduce the residual stresses and distortions. Mugwagwa et al. [28] indeed showed that successive chessboard strategies (scanning in a chessboard fashion by first melting the horizontal sub-sectors then the vertical sub-sectors) was more effective than island strategies (scanning in a random manner).

A more universal model should strictly take into account other process parameters influencing the distortion (such as the power bed temperature, down or inter-layer time, material properties, part geometry, number of layers, supporting structures, etc.), which is not trivial. The effect of the scanning orientation of the last layer with respect to the specimen geometry could be taken into account by using $K_{\max}$ as a criterion (Fig. 17). To account for other process parameters (including E_v, pre-heating, downtime, scanning strategy or vector length), it is suggested to consider their respective effect on the transient heat transfer during the deposition of the last layer.

An attempt of such uniformization of the problem was recently proposed by Fergani et al. [65] to predict the residual stresses in additive manufacturing of metallic components. This approach, based on a thermo-elastic model using Timoshenko analysis of an isothermal bi-layered slab with two different expansion coefficients, consisted to replace Timoshenko's slab by one with the same expansion coefficients, but two different temperatures (the cold one representing the previously melted layer and the hot one the last deposited layer). The source of distortion would then come from the thermal gradient ($\alpha.\Delta T$) instead of the heterogeneity of the expansion coefficient ($\Delta\alpha.T$). Such an approach was interesting to show the effect of the thickness of the last layer or the preheating. However, it could not be used to examine the effect of the volumetric energy density or the scanning strategy (other than the orientation of the last layer). Indeed, it does not take into account the transient heat transfer which takes place during the deposition.

Another approach, based on thermal stresses in slabs and transient heat transfer, is therefore required. As a first step, a thermo-elastic model could suffice, like the Timoshenko one. In a previous study [66], it has been revealed that the distortion or curvature of a slab subjected to a transient power input on one side could be normalized using the following parameters:

- the heat power density ($W.m^{-2}$),
- the duration of the power application (s),
- the slab material properties (Young's modulus E, thermal expansion coefficient α, Poisson coefficient ν, thermal conductivity λ, thermal diffusivity κ),
- the thickness of the slab (m).

The heat transfer coefficient of a cooling fluid on the back face was also included in the normalization and in the analytical model. An example of application of this approach was illustrated in Figure 18 for a die-casting case [66], where the normalized radius of curvature (the inverse of the curvature) of the slab was plotted as a function of the normalized time for different coefficients of cooling heat transfer. The interruption of the heat power and the return of the radius of curvature towards the initial infinite value was shown by the curves of different colors with the power switch off time noted as τ^+. The effect of the cooling heat transfer coefficient was indicated by the different curve labels. It was only in the slowest cooling condition (*h*$^+$=1) that the return to flatness of the slab was significantly fastest. With stronger cooling, a temperature gradient was maintained longer and the difference was noticeable only after a normalized time of 0.5, which represents the diffusion time through the slab (only then had the back face cooling an effect).

An interesting approach for the case of the SLM process would consist in relating the deposition strategy and process parameters in terms of heat power density, an equivalent time of deposition, the initial temperature of the cold face, the thickness of the slab before the deposition and the thermo-mechanical properties of the material, using the same normalization principles. The challenge would be to relate all the scanning strategies to an equivalent time of deposition, and to account for the cohesive temperature of the material once sufficiently solid. This approach, which remains to be developed, will be the subject of future work.

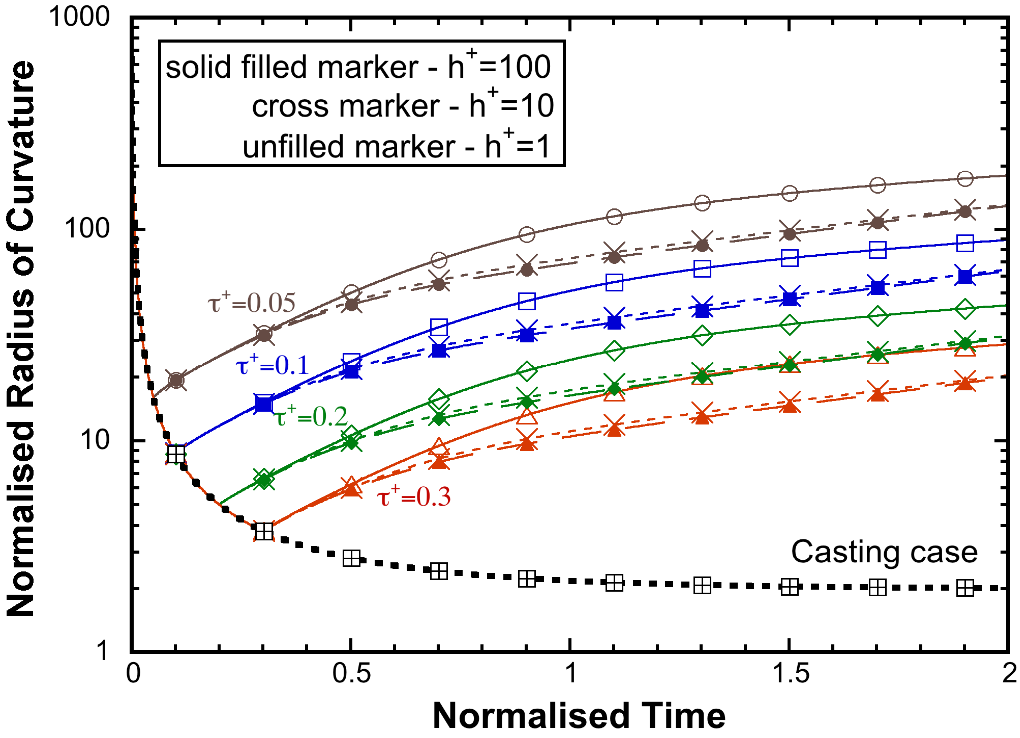

Fig. 18 – An example of application of the normalized approach based on transient heat transfer: evolution of the normalized radius of curvature of a slab as a function of the normalized time, for different coefficients of cooling heat transfer h^+ and power switch off time τ^+ [66].

5. Conclusions

The purpose of this study was to determine the influence of the process parameters, in particular the energy density, the geometry and the scanning strategy, on the residual stresses related distortion in Ti–6Al–4V parts produced by Selective Laser Melting. Based on an improvement of the Bridge Curvature Method (BCM) which consists in determining the distortion of a bridge specimen after separation of the support plate, criteria such as the maximum curvature ($K_{\max}$) and its orientation were determined from 3D topographic measurements of the upper surface. The following conclusions and perspectives could be drawn from this study:

- Comparison with the literature revealed that the distortion measurement method and associated evaluation criteria could bias the residual stress analysis. While 2D methods such as measuring the deflection angle of the lower pillars tend to over-estimate the distortions, the improved BCM used here allowed the direction of the maximum distortion (and therefore the anisotropy of the stress state) to be unambiguously determined.
- It was shown that the main curvature resulting from the release of residual stresses was generally aligned along the scanning direction, except for experiments conducted at low scanning speed (<1000 mm.s^{-1}). Higher scanning speeds cause the melt pool to elongate and increase the thermal gradients, and thus the anisotropy of residual stresses. As for the laser power, it enlarges the melt in all directions, only slightly impacting the stress anisotropy at low speed.
- Increasing the volumetric energy density E_v in the range [18-57 J.mm^{-3}], keeping the same scanning strategy, allowed to reduce the distortion which reached an asymptotic minimum above a critical E_v. However, the energy density remains an engineering parameter whose relevance was not clearly demonstrated.
- The scanning strategy has been shown to have a significant impact on residual stresses, those involving longer vector lengths giving rise to maximum deformation. Reducing the length of the scan vectors from 20 mm to 2.5 mm allowed to reduce distortion by almost 50%, with a more effective effect below 5 mm. For a given E_v, a power law has been found to relate the maximum curvature $K_{\max}$ to the average length of the scan vectors induced by the scanning strategy.
- The hatch rotation strategy, i.e. the alternating rotation of the scanning direction from one layer to another between 0° and β, showed no difference with the unidirectional zigzag strategy oriented at $\theta=\beta$, since the last layer (melted using a β scanning orientation) plays a predominant role on the distortion of the upper surface. In fact, the effect of the rotation of the scanning orientation could be explained by a change in the

mean vector length (determined here by a trigonometric approach), especially for specimens with an asymmetrical shape such as the conventional bridge specimens.

- The specimen geometry should be taken into account when analyzing the results, as this may lead to favor the distortion according to preferential directions of low stiffness. The use of axisymmetric shape specimen consistent with the principle of the curvature method should prevent this problem.
- When designing a part for an industrial application, it may be recommended to favor symmetrical shapes and to select judiciously the orientation of the scanning according to the local geometry, with the aim of reducing the residual stresses generated during the manufacturing.
- The main guidelines of an analytical approach for predicting the curvature resulting from thermal stresses, were drawn. This model, based on the transient heat transfer during the deposition of the last layer, should take into account all the process parameters (such as the energy density, pre-heating, downtime, vector length), through the consideration of the heat power density and an equivalent deposition time. This will be the subject of future work.

Acknowledgments

The authors would like to thank the CIRIMAT, and especially Vincent Baylac, for providing SLM specimens. Moreover, Kévin Grondin is greatly acknowledged for its contribution to the development of the Matlab® routine.

Appendix A. Calculation of the maximum and mean length of scan vectors

Table A1

Theoretical maximum and mean lengths of scan vectors achieved with different laser scanning orientations.

Laser orientation θ (°)	0 (Ref.)	15	30	45	60	75	90
Maximum length L_{max} (mm)	20.0	20.7	20.0	14.1	11.6	10.3	10.0
Mean length L_{m} (mm)	20.0	13.5	10.8	9.4	8.9	9.1	10.0

Appendix B. Results of distortion measurements

Table B1

Distortion parameters measured on conventional bridge specimens built with various laser powers and scanning speeds.

Laser power P (W)	100	200	200	300	300	300
Scanning speed v (mm.s^{-1})	600	600	1800	900	1800	2700
Total flatness deviation $FLTt$ (µm)	173	132	231	99	188	207
Quadratic flatness deviation $FLTq$ (µm)	41	25	59	25	53	58
Maximum curvature $K_{\max}$ (mm^{-1})	3.18	6.50	4.11	1.79	3.82	4.14
Mean curvature K_m (mm^{-1})	2.95	3.71	3.80	0.77	2.25	2.69
Minimum curvature $K_{\min}$ (mm^{-1})	2.71	0.91	3.49	-0.24	0.68	1.24
Orientation of the curvature $O_{\max}$ (°)	27.6	176.9	87.6	101.7	89.3	90.2

Table B2
Distortion parameters measured on conventional bridge specimens built with various laser scanning orientations.

Laser scanning orientation θ (°)	0 (Ref.)	15	30	45	60	75	90
Total flatness deviation $FLTt$ (µm)	205	197	186	180	150	130	110
Quadratic flatness deviation $FLTq$ (µm)	55	49	44	38	30	25	23
Maximum curvature $K_{\max}$ (mm^{-1})	3.95	3.58	3.27	3.20	2.93	2.94	3.01
Mean curvature K_m (mm^{-1})	2.62	2.30	2.20	1.90	2.15	2.15	2.22
Minimum curvature $K_{\min}$ (mm^{-1})	1.29	1.02	1.13	0.60	1.35	1.36	1.44
Orientation of the curvature $O_{\max}$ (°)	93.0	101.1	109.1	125.8	142.3	163.9	178.8

Table B3
Distortion parameters measured on conventional bridge specimens built with various hatch angles.

Hatch angle β (°)	0 (Ref.)	30	45	90	105	150
Total flatness deviation $FLTt$ (µm)	205	189	171	93	117	198
Quadratic flatness deviation $FLTq$ (µm)	55	43	35	20	24	46
Maximum curvature $K_{\max}$ (mm^{-1})	3.95	3.28	3.32	3.17	2.91	3.45
Mean curvature K_m (mm^{-1})	2.62	2.39	2.56	2.21	2.09	2.61
Minimum curvature $K_{\min}$ (mm^{-1})	1.29	1.48	1.81	1.24	1.52	1.77
Orientation of the curvature $O_{\max}$ (°)	93.0	115.3	144.5	180.4	196.1	247.5

Table B4

Distortion parameters measured on conventional bridge specimens built with various lengths of scan vectors.

Length of scan vectors L_v (mm)	2.5	5	10	20 (Ref.)
Total flatness deviation $FLTt$ (µm)	119	162	174	205
Quadratic flatness deviation $FLTq$ (µm)	31	44	47	55
Maximum curvature $K_{\max}$ (mm^{-1})	2.17	3.16	3.39	3.95
Mean curvature K_m (mm^{-1})	1.81	2.24	2.30	2.62

Minimum curvature K_{min} (mm^{-1})	1.44	1.33	1.22	1.29
Orientation of the curvature O_{max} (°)	87.5	91.1	88.2	93.0

Table B5

Distortion parameters measured on conventional bridge specimens built with a concentric scanning.

Concentric scanning	Inwards	Outwards
Total flatness deviation *FLTt* (µm)	204	128
Quadratic flatness deviation *FLTq* (µm)	54	34
Maximum curvature K_{max} (mm^{-1})	3.80	2.41
Mean curvature K_{m} (mm^{-1})	3.01	0.51
Minimum curvature K_{min} (mm^{-1})	2.22	-1.39
Orientation of the curvature O_{max} (°)	91.6	91.9

Table B6

Distortion parameters measured on rectangular and square-based bridge specimens built using the reference scanning strategy.

Specimen base shape	Rectangular	Square	
Number of holes	Single	Single	Double
Total flatness deviation *FLTt* (µm)	188	187	238
Quadratic flatness deviation *FLTq* (µm)	53	52	58
Maximum curvature K_{max} (mm^{-1})	3.82	3.72	4.05
Mean curvature K_{m} (mm^{-1})	2.25	1.95	2.55
Minimum curvature K_{min} (mm^{-1})	0.68	0.18	1.05
Orientation of the curvature O_{max} (°)	89.3	90.9	89.7

References

[1] B. Vandenbroucke, J.P. Kruth. Selective laser melting of biocompatible metals for rapid manufacturing of medical parts. Rapid Prototyp. J. 13(4) (2007), 196–203.

[2] P. Mercelis, J.-P. Kruth, Residual stresses in selective laser sintering and selective laser melting. Rapid Prototyp. J. 12(5) (2006) 254–265.

[3] B. Vrancken, Study of residual stresses in selective laser melting (2016).

[4] J.-P. Kruth, J. Deckers, E. Yasa, R. Wauthlé, Assessing and comparing influencing factors of residual stresses in selective laser melting using a novel analysis method. Proc. Inst. Mech. Eng. Part B J. Eng. Manuf. 226(6) (2012) 980–991.

[5] I. Yadroitsava, S. Grewar, D. Hattingh, I. Yadroitsev, Residual stress in SLM Ti6Al4V alloy specimens. Mater. Sci. Forum 828 (2015), 305–310.

[6] S. Liu, Y. C. Shin, Additive manufacturing of Ti6Al4V alloy: a review. Mater. Design 164 (2019) 107552.

[7] L. Mugwagwa, D. Dimitrov, S. Matope, R. Muvunzi, Residual stresses and distortions in selective laser melting – A review. In: Proceedings of the 17th International Conference of the Rapid Product Development of South Africa, November 2016.

[8] H. Shipley, D. McDonnell, M. Culleton, R. Coull, R. Lupoi, G. O'Donnell, D. Trimble, Optimisation of process parameters to address fundamental challenges during selective laser melting of Ti-6Al-4V: A review. Int. J. Machine Tools Manuf.128 (2018) 1–20.

[9] C. Li, Z.Y. Liu, X.Y. Fang, Y.B. Guo, Residual stress in metal additive manufacturing. Procedia Cirp 7(2018) 348-353.

[10] A.S. Wu, D.W. Brown, M. Kumar, G.F. Gallegos, W.E. King, An experimental investigation into additive manufacturing-induced residual stresses in 316L stainless steel. Metall. Mater. Trans. A 45(13) (2014) 6260–6270.

[11] L. Mugwagwa, D. Dimitrov, S. Matope, I. Yadroitsev, Influence of process parameters on residual stress related distortions in selective laser melting. Procedia Manufacturing 21 (2018) 92–99.

[12] M. Malý, C. Höller, M. Skalon, B. Meier, D. Koutný, R. Pichler, C. Sommitsch, D. Paloušek, Effect of process parameters and high-temperature preheating on residual stress and relative density of Ti6Al4V processed by selective laser melting, Mater. 12 (2019) 930.

[13] Y. Liu, Y. Yang, D. Wang, A study on the residual stress during selective laser melting (SLM) of metallic powder. Int. J. Adv. Manuf. Technol. 87(1-4) (2016) 647–656.

[14] T. Mishurova, S. Cabeza, K. Artzt, J. Haubrich, M. Klaus, C. Genzel, G. Requena, G. Bruno, An Assessment of Subsurface Residual Stress Analysis in SLM Ti-6Al-4V. Materials 10(4) (2017) 348.

[15] H. Pohl, A. Simchi, M. Issa, H.C. Dias, Thermal stresses in direct metal laser sintering. In: Proceedings of SFF Symp., 2001, pp. 366–372.

[16] L. Van Belle, G. Vansteenkiste, J.C. Boyer. Investigation of residual stresses induced during the selective laser melting process. Key Eng. Mater. 554–557 (2013) 1828–34.

[17] M.F. Zaeh, G. Branner, Investigations on residual stresses and deformations in selective laser melting. Prod. Eng. 4(1) (2010) 35–45.

[18] A.H. Nickel, D.M. Barnett, F.B. Prinz, Thermal stresses and deposition patterns in layered manufacturing, Mater. Sci. Eng. A 317 (2001) 59–64.

[19] J.P. Kruth, L. Froyen, J. Van Vaerenbergh, P. Mercelis, M. Rombouts, B. Lauwers, Selective laser melting of iron-based powder. J. Mater. Process. Technol. 149(1) (2004) 616–622.

[20] J. Jhabvala, E. Boillat, T. Antignac, R. Glardon, On the effect of scanning strategies in the selective laser melting process. Virtual Phys. Prototyp. 5(2) (2010) 99–109.

[21] Q. Bo, S. Yu-sheng, W. Qing-song, W. Hai-bo, The helix scan strategy applied to the selective laser melting. Int. J. Adv. Manuf. Technol. 63(5-8) (2012) 631–640.

[22] A.J. Dunbar, E.R. Denlinger, J. Heigel, P. Michaleris, P. Guerrier, R. Martukanitz, T.W. Simpson, Development of experimental method for in situ distortion and temperature measurements during the laser powder bed fusion additive manufacturing process. Addit. Manuf. 12 (2016) 25–30.

[23] S.D. Bagg, L.M. Sochalski-Kolbus, J.R. Bunn, The effect of laser scan strategy on distortion and residual stresses of arches made with selective laser melting. 2016, NASA report M16-5377.

[24] H. Ali, L. Ma, H. Ghadbeigi, K. Mumtaz, In-situ residual stress reduction, martensitic decomposition and mechanical properties enhancement through high temperature powder bed pre-heating of Selective Laser Melted Ti6Al4V. Mater. Sci. Eng. A 695 (2017) 211–220.

[25] H. Ali, H. Ghadbeigi, K. Mumtaz, Effect of strategies on residual stress and mechanical properties of Selective Laser Melted Ti6Al4V. Mater. Sci. Eng. A 712 (2018) 175–187.

[26] N. Nadammal, S. Cabeza, T. Mishurova, T. Thiede, A. Kromm, C. Seyfert, L. Farahbod, C. Haberland, J.A. Schneider, P. Dolabella Portella, G. Bruno, Effect of hatch length on the development of microstructure, texture and residual stresses in selective laser melted superalloy Inconel 718. Mater. Design 134 139–150.

[27] J. Robinson, I. Ashton, P. Fox, E. Jones, C. Sutcliffe, Determination of the effect of scan strategy on residual stress in laser powder bed fusion additive manufacturing. Addit. Manuf. 23(2018) 13–24.

[28] L. Mugwagwa, D. Dimitrov, S. Matope, I. Yadroitsev, Evaluation of the impact of scanning strategies on residual stresses in selective laser melting. Int. J. Advanced Manufacturing Technol. 102 (2019) 2441–2450.

[29] M. Shiomi, K. Osakada, K. Nakamura, T. Yamashita, F. Abe, Residual stress within metallic model made by selective laser melting process. Cirp Annals 53(1) (2004) 195–198.

[30] T. Furumoto, T. Ueda, A. Aziz, M. Sanusi, A. Hosokawa, R. Tanaka, Study on reduction of residual stress induced during rapid tooling process: Influence of heating conditions on residual stress. Key Eng. Mater. 447 (2010) 785–789.

[31] D. Buchbinder, W. Meiners, N. Pirch, K. Wissenbach, J. Schrage. Investigation on reducing distortion by preheating during manufacture of aluminum components using selective laser melting. J. Laser Appl. 26(1) (2014) 12004.

[32] S. Bremen, W. Meiners, A. Diatlov, Selective laser melting: a manufacturing technology for the future? Laser Technik J. 9(2) (2012) 33–38.

[33] B. Zhang, L. Dembinski, C. Coddet, The study of the laser parameters and environment variables effect on mechanical properties of high compact parts elaborated by selective laser melting 316L powder. Mater. Sci. Eng. A 584 (2013) 21–31.

[34] J. Cao, M.A. Gharghouri, P. Nash, Finite-element analysis and experimental validation of thermal residual stress and distortion in electron beam additive manufactured Ti-6Al-4V build plates. J. Mater. Processing Technol. 237(2016) 409–419.

[35] E.R. Denlinger, J.C. Heigel, P. Michaleris, T.A. Palmer, Effect of inter-layer dwell time on distortion and residual stress in additive manufacturing of titanium and nickel alloys. J. Mater. Processing Technol. 215 (2015) 123–131.

[36] C. Casavola, S.L. Campanelli, C. Pappalettere, Preliminary investigation on distribution of residual stress generated by the selective laser melting process. J. Strain Analysis Eng. Design 44(1) (2009) 93–104.

[37] I. Yadroitsev, I. Yadroitsava, Evaluation of residual stress in stainless steel 316L and Ti6Al4V samples produced by selective laser melting. Virtual Physical Prototyp. 10(2) (2015) 67–76.

[38] E.R. Denlinger, J.C. Heigel, P. Michaleris, Residual stress and distortion modeling of electron beam direct manufacturing Ti-6Al-4V. In: Proceedings of the Institution of Mechanical Engineers, Part B: J. Eng. Manuf. 229(10) (2015) 1803–1813.

[39] L. Papadakis G. Branner, A. Schober, K.H. Richter, T. Uihlein, Numerical modeling of heat effects during thermal manufacturing of aero engine components. In: Proceedings of the World Congress on Engineering, Vol. 3 (2012).

[40] A. Hussein, L. Hao, C. Yan, R. Everson, P. Young, Advanced lattice support structures for metal additive manufacturing. J. Mater. Processing Technol. 213(7) (2013) 1019–1026.

[41] A. Salmi, E. Atzeni, L. Iuliano, M. Galati, Experimental analysis of residual stresses on AlSi10Mg parts produced by means of Selective Laser Melting (SLM), Procedia Cirp 62 (2017) 458–463.

[42] T. Mishurova, S. Cabeza, T. Thiede, N. Nadammal, A. Kromm, M. Klaus, C. Genzel, C. Haberland, G. Bruno, The influence of the support structure on residual stress and distortion in SLM Inconel 718 parts. Metall. Mater. Trans. A 3038 (49A) (2018).

[43] T. Vilaro, C. Colin, J.D. Bartout. As-fabricated and heat-treated microstructures of the Ti-6Al-4V alloy processed by selective laser melting. Metall. Mater. Trans. A Phys. Metall. Mater. Sci. 42 (2011) 3190–3199.

[44] M. Simonelli, Y.Y. Tse, C. Tuck. Effect of the build orientation on the mechanical properties and fracture modes of SLM Ti–6Al–4V. Mater. Sci. Eng. A 616 (2014) 1–11.

[45] P.J. Withers, H.K.D.H. Bhadeshia, Residual stress. Part 1–measurement techniques. Mater. Sci. Technol. 17(4) (2001) 355–365.

[46] S. Le Roux, M. Salem, A. Hor, Improvement of the bridge curvature method to assess residual stresses in selective laser melting. Addit. Manuf. 22 (2018) 320–329.

[47] K.G. Prashanth, S. Scudino, T. Maity, J. Das, J. Eckert, Is the energy density a reliable parameter for materials synthesis by selective laser melting? Mater. Res. Lett. 5(6) (2017) 386–390.

[48] V. Gunenthiram, Compréhension de la formation de porosités en fabrication additive (LBM). Analyse expérimentale de l'interaction laser–lit de poudre–bain liquide. Doctoral dissertation, Paris, ENSAM 2018.

[49] A. Roberts, Curvature attributes and their application to 3D interpreted horizons. First break 19(2) (2001) 85–100.

[50] L. Papadakis, A. Loizou, J. Risse, J. Schrage, Numerical computation of component shape distortion manufactured by selective laser melting. Procedia Cirp 18 (2014) 90–95.

[51] C. Li, C.H. Fu, Y.B. Guo, F.Z. Fang, A multiscale modeling approach for fast prediction of part distortion in selective laser melting. J. Mater. Proc. Technol. 229 (2016) 703–712.

[52] L. Thijs, F. Verhaeghe, T. Craeghs, J. Van Humbeeck, J.P. Kruth, A study of the microstructural evolution during selective laser melting of Ti–6Al–4V. Acta Mater. 58(9) (2010) 3303–3312.

[53] L. Thijs, M.L.M. Sistiaga, R. Wauthle, Q. Xie, J.P. Kruth, J. Van Humbeeck, Strong morphological and crystallographic texture and resulting yield strength anisotropy in selective laser melted tantalum. Acta Mater. 61(12) (2013) 4657–4668.

[54] K. Guan, Z. Wang, M. Gao, X. Li, X. Zeng, Effects of processing parameters on tensile properties of selective laser melted 304 stainless steel. Mater. Design 50 (2013) 581–586.

[55] P. Hanzl, M. Zetek, T. Bakša, T. Kroupa, The influence of processing parameters on the mechanical properties of SLM parts. Procedia Eng. 100(1) (2015) 1405–1413.

[56] J.H. Robinson, I.R.T. Ashton, E. Jones, P. Fox, C. Sutcliffe, The effect of hatch angle rotation on parts manufactured using selective laser melting. Rapid Prototyp. J. 25(2) (2019) 289–298.

[57] P. Edwards, M. Ramulu, Fatigue performance evaluation of selective laser melted Ti–6Al–4V. Mater. Sci. Eng. A 598 (2014) 327–337.

[58] C. Li, J.F. Liu, Y.B. Guo, Prediction of residual stress and part distortion in selective laser melting. Procedia Cirp 45 (2016) 171–174.

[59] L. Parry, I.A. Ashcroft, R.D. Wildman, Understanding the effect of laser scan strategy on residual stress in selective laser melting through thermo-mechanical simulation. Addit. Manuf. 12 (2016) 1–15.

[60] G. Kasperovich, G.J. Haubrich, J. Gussone, G. Requena, Correlation between porosity and processing parameters in TiAl6V4 produced by selective laser melting. Mater. Design 105 (2016) 160–170.

[61] U.S. Bertoli, A.J. Wolfer, M.J. Matthews, J.P.R. Delplanque, J.M. Schoenung, On the limitations of volumetric energy density as a design parameter for selective laser melting. Mater. Design 113 (2017) 331–340.

[62] L. Ma, H. Bin, Temperature and stress analysis and simulation in fractal scanning-based laser sintering. Int. J. Adv. Manuf. Technol. 34(9-10) (2007) 898–903.

[63] L. Parry, I.A. Ashcroft, R.D. Wildman, Geometrical effects on residual stress in selective laser malting. Addit. Manuf. 25 (2019) 166–175.

[64] B. Cheng, S. Shrestha, K. Chou, Stress and deformation evaluations of scanning strategy effect in selective laser melting. Addit. Manuf. (2016).

[65] O. Fergani, F. Berto, T. Welo, S.Y. Liang Analytical modelling of residual stress in additive manufacturing. Fatigue Fracture Eng. Mater. Structures 40(6) (2017) 971–978.

[66] G. Dour (2001), Thermal stresses and distortion in dies of die casting processes: a new normalized approach. Modelling Simul. Mater. Sci. Eng. 9(5) 399–413.

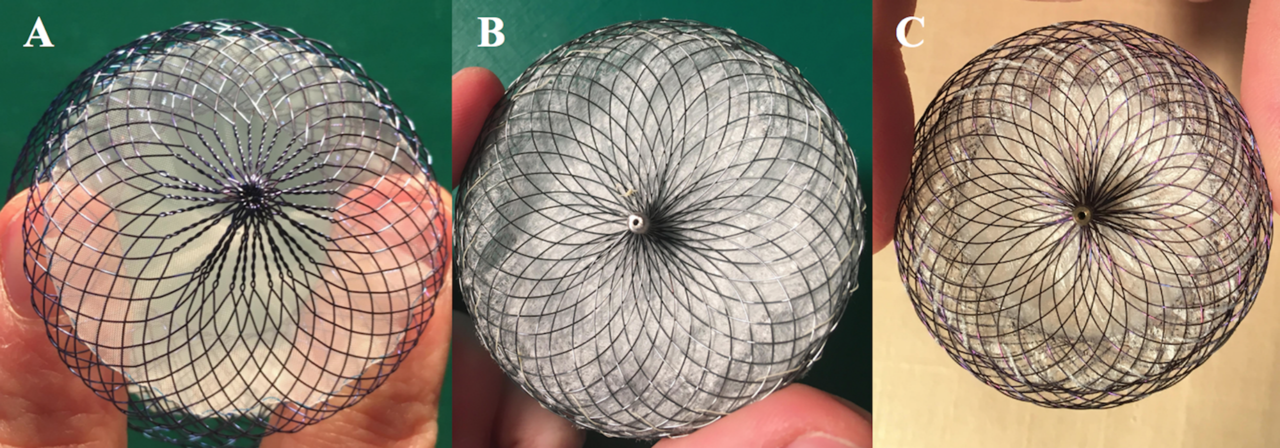
A
B
C

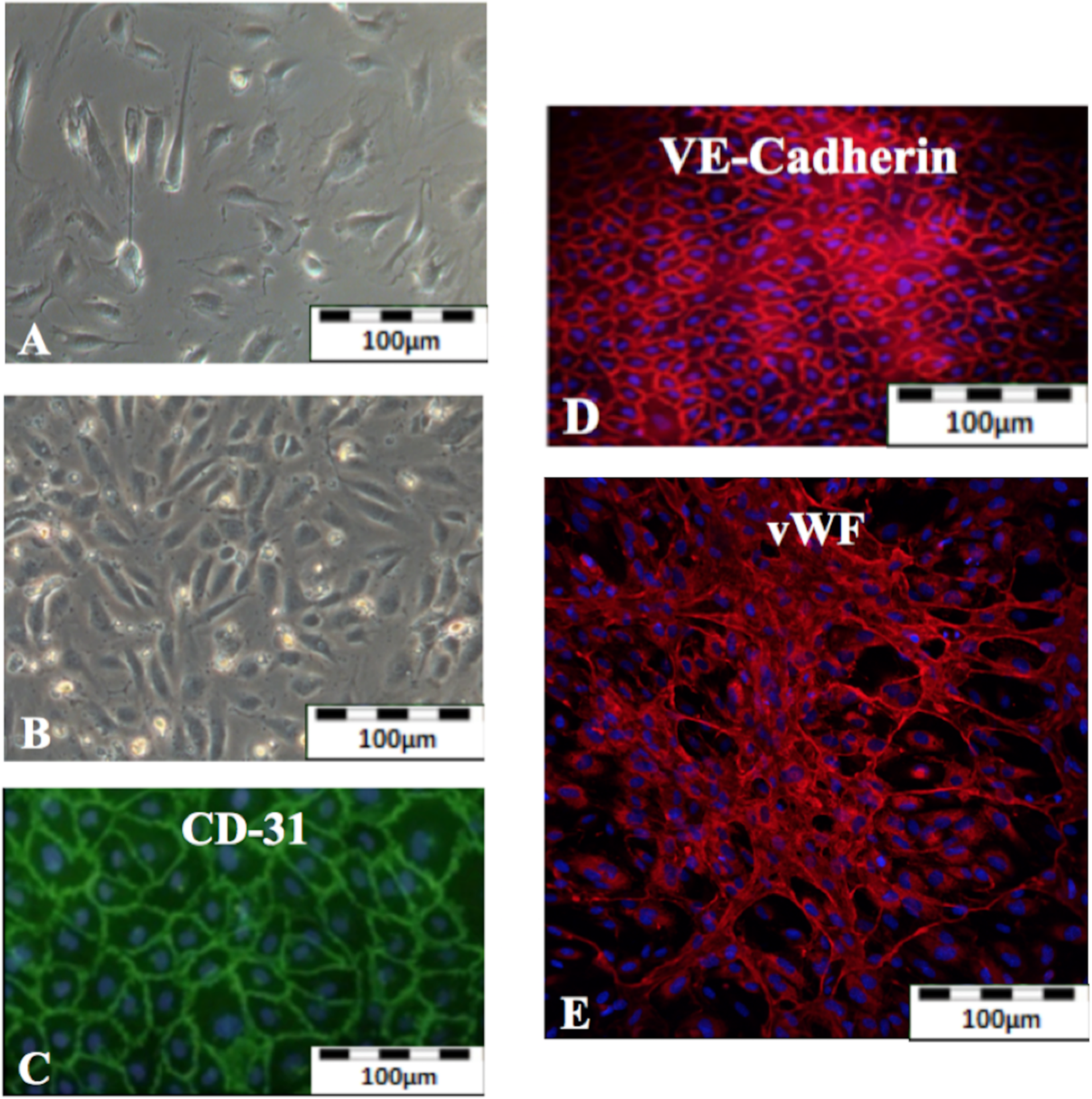
A
100µm
B
100µm
CD-31
C
100µm
VE-Cadherin
D
100µm
vWF
E
100µm

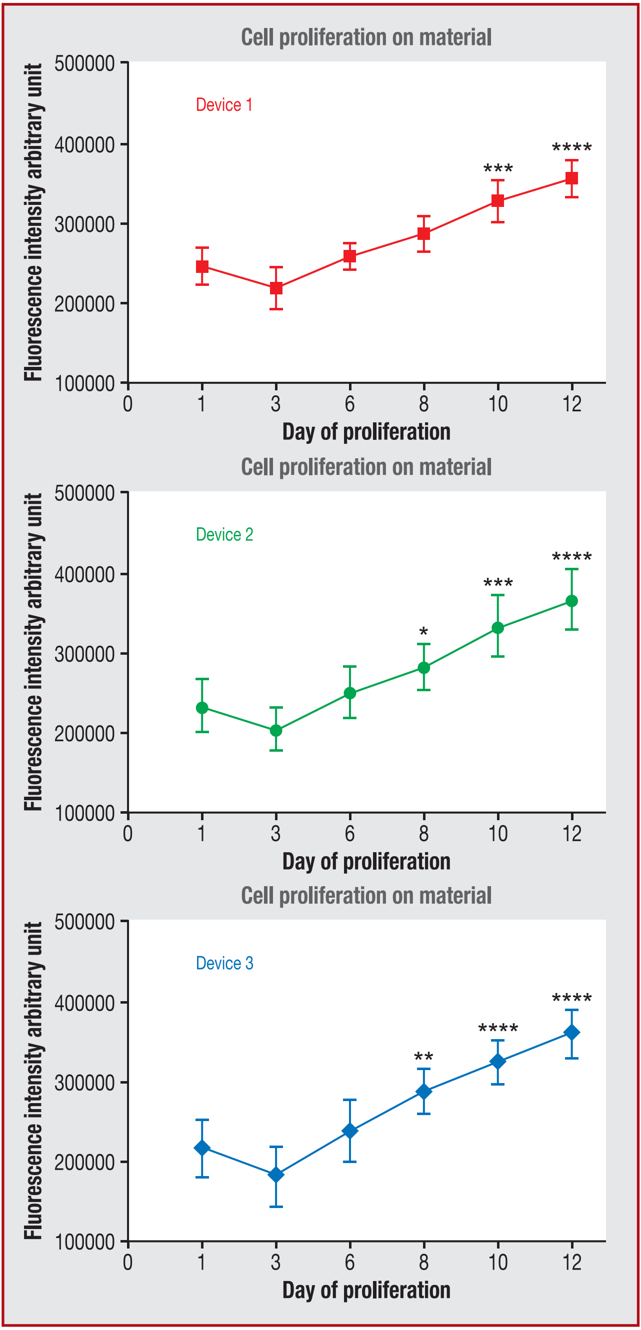
Cell proliferation on material
Device 1
Fluorescence intensity arbitrary unit
500000
400000
300000
200000
100000
0
1
3
6
8
10
12
***
****
Day of proliferation
Cell proliferation on material
Device 2
Fluorescence intensity arbitrary unit
500000
400000
300000
200000
100000
0
1
3
6
8
10
12
*
***
****
Day of proliferation
Cell proliferation on material
Device 3
Fluorescence intensity arbitrary unit
500000
400000
300000
200000
100000
0
1
3
6
8
10
12
**
****
****
Day of proliferation

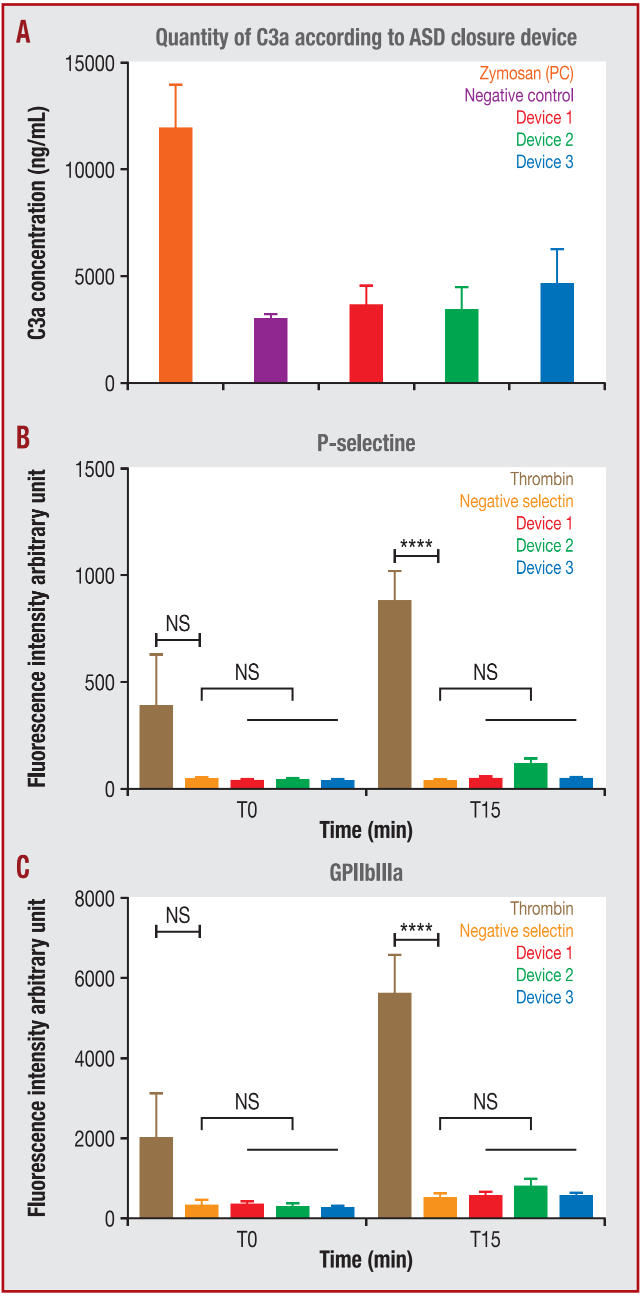

A Quantity of C3a according to ASD closure device

B P-selectine

C GPIIbIIIa

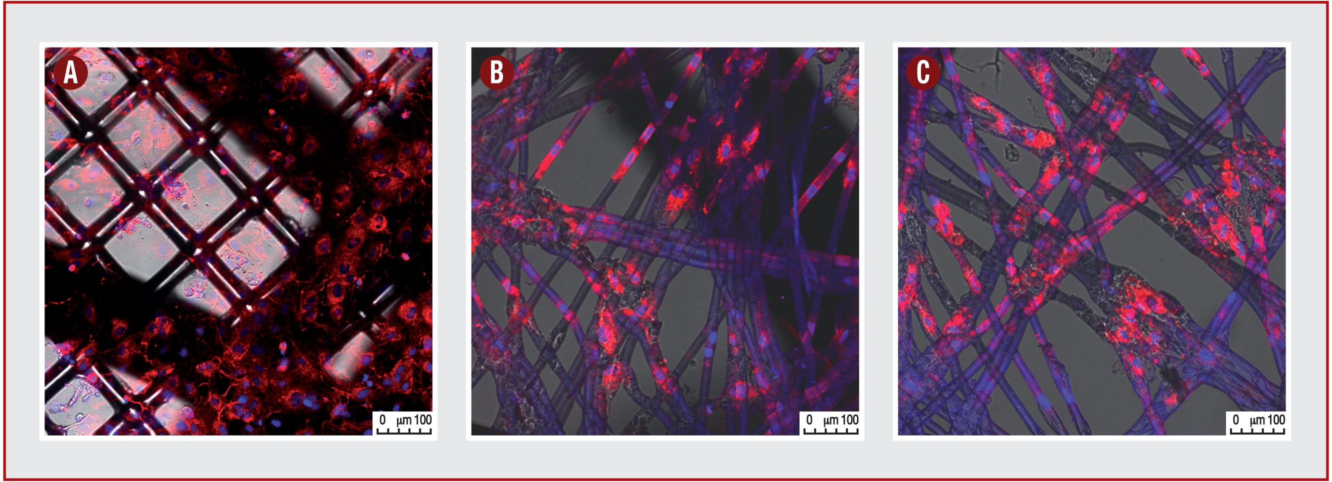
A
0 µm 100
B
0 µm 100
C
0 µm 100